Sidewall Effects on Exact Reynolds-Stress Budgets in an Impinging Shock Wave/Boundary Layer Interaction

Manan A. Vyas and Dennis A. Yoder
Glenn Research Center, Cleveland, Ohio

Datta V. Gaitonde
The Ohio State University, Columbus, Ohio

NASA STI Program . . . in Profile

Since its founding, NASA has been dedicated to the advancement of aeronautics and space science. The NASA Scientific and Technical Information (STI) Program plays a key part in helping NASA maintain this important role.

The NASA STI Program operates under the auspices of the Agency Chief Information Officer. It collects, organizes, provides for archiving, and disseminates NASA's STI. The NASA STI Program provides access to the NASA Technical Report Server—Registered (NTRS Reg) and NASA Technical Report Server—Public (NTRS) thus providing one of the largest collections of aeronautical and space science STI in the world. Results are published in both non-NASA channels and by NASA in the NASA STI Report Series, which includes the following report types:

- TECHNICAL PUBLICATION. Reports of completed research or a major significant phase of research that present the results of NASA programs and include extensive data or theoretical analysis. Includes compilations of significant scientific and technical data and information deemed to be of continuing reference value. NASA counter-part of peer-reviewed formal professional papers, but has less stringent limitations on manuscript length and extent of graphic presentations.

- TECHNICAL MEMORANDUM. Scientific and technical findings that are preliminary or of specialized interest, e.g., "quick-release" reports, working papers, and bibliographies that contain minimal annotation. Does not contain extensive analysis.

- CONTRACTOR REPORT. Scientific and technical findings by NASA-sponsored contractors and grantees.

- CONFERENCE PUBLICATION. Collected papers from scientific and technical conferences, symposia, seminars, or other meetings sponsored or co-sponsored by NASA.

- SPECIAL PUBLICATION. Scientific, technical, or historical information from NASA programs, projects, and missions, often concerned with subjects having substantial public interest.

- TECHNICAL TRANSLATION. English-language translations of foreign scientific and technical material pertinent to NASA's mission.

For more information about the NASA STI program, see the following:

- Access the NASA STI program home page at http://www.sti.nasa.gov

- E-mail your question to help@sti.nasa.gov

- Fax your question to the NASA STI Information Desk at 757-864-6500

- Telephone the NASA STI Information Desk at 757-864-9658

- Write to:
  NASA STI Program
  Mail Stop 148
  NASA Langley Research Center
  Hampton, VA 23681-2199

Sidewall Effects on Exact Reynolds-Stress Budgets in an Impinging Shock Wave/Boundary Layer Interaction

Manan A. Vyas and Dennis A. Yoder
Glenn Research Center, Cleveland, Ohio

Datta V. Gaitonde
The Ohio State University, Columbus, Ohio

National Aeronautics and
Space Administration

Glenn Research Center
Cleveland, Ohio 44135

March 2019

Acknowledgments

Sidewall Effects on Exact Reynolds-Stress Budgets in an Impinging Shock Wave/Boundary Layer Interaction

Manan A. Vyas and Dennis A. Yoder
National Aeronautics and Space Administration
Glenn Research Center
Cleveland, Ohio 44135

Datta V. Gaitonde
The Ohio State University
Columbus, Ohio 43210

Abstract

Large-eddy simulations are performed using wall-resolved mesh for a Mach 2.29 impinging shock wave/boundary-layer interaction. Flow conditions are based on an experiment and therefore entire span was simulated, including the two sidewalls. Mean flow comparison with the experimental data showed that the predicted interaction length was larger in the simulation. Time-series analysis of a rake of pressure signals immediately downstream of the mean reflected shock position showed a peak in weighted power spectral density occurred about $St_{Lint} = 0.01$, owing to a larger interaction length. Budgets of Reynolds-stress transport calculated across the span and along the corner bisector showed high degree of anisotropy. Merging of the secondary flows and separation along the corner gave rise to unstable counter-rotating vortices, which straddle the corner and grow in size. This also leads to a development of new behavior in the viscous sublayer along the corner bisector, where the pressure strain and molecular diffusion mechanisms become prominent.

Nomenclature

δ_{99}	boundary-layer thickness
δ_{ij}	Kronecker delta
ϵ_{ij}	dissipation tensor
γ	specific heat ratio
κ	thermal conductivity constant or Kármán constant
$\mathcal{D}_{ij}^{\nu}$	molecular diffusion tensor
$\mathcal{D}_{ij}^{P}$	pressure diffusion tensor
$\mathcal{D}_{ij}^{T}$	turbulent diffusion tensor
$\mathcal{D}_{ij}$	diffusion tensor (total)
$\mathcal{M}_{ij}$	turbulent mass flux tensor
$\mathcal{P}_{ij}$	production tensor
μ	molecular viscosity
Π_{ij}	pressure strain tensor
ρ	density
τ_{ij}	Reynolds-stress tensor
θ	boundary-layer momentum thickness
ζ	second viscosity
B	law of the wall intercept constant
C_p	specific heat at constant pressure
e	internal energy
e_0	total energy

I_x, I_y, I_z	digital filter length scale in x, y, and z directions, respectively
L	length scale
M	Mach number
N_y, N_z	digital filter size in y and z directions
p	pressure
Pr	Prandtl number
Re	Reynolds number
s_{ij}	instantaneous strain-rate tensor
T	temperature
t	time
$t_{ij}, \boldsymbol{t}$	viscous stress tensor
u, v, w	non-dimensional velocity in x, y, and z directions, respectively
V	velocity magnitude
x, y, z	non-dimensional coordinates

Subscripts

0	total condition
c	centerline
exp	experiment
i, j, k	index notation, equal to 1, 2, or 3
imp	impingement location
int	interaction
ref, ∞	reference value same as freestream value
sep	separation
sim	simulation
w	wall

Conventions

$^{-}$	Reynolds averaged
$\sim$	Favre averaged

Superscripts

$'$	Reynolds decomposition
$''$	Favre decomposition
$*$	non-dimensional value

I.   Introduction

Experimental, numerical, and modeling studies of shock wave/boundary-layer interactions (SBLIs) in a variety of configurations can be found in the literature.[1–3] SBLIs are present in transonic, supersonic, and hypersonic speed regimes and thus relevant to commercial, military, and space vehicles of the past, present, and future. SBLIs create excessive unsteady aerothermal loads that can compromise structural integrity, result in component failure, and lead to loss of control. In the propulsion flowpath, the adverse pressure gradient due to SBLI can cause flow separation, distortion, and loss in engine efficiency. Due to these critical characteristics, SBLIs are one of the most actively researched phenomena in high speed flows.

SBLIs exhibit low-frequency unsteadiness and three-dimensional (3D) separation, often including corner separation owing to rectangular flowpaths, which make their prediction extremely difficult. While investigating the low-frequency unsteadiness[1,4,5] of the reflected shock in an SBLI is important to design flow control mechanisms, charaterizing the local anisotropic and inhomogeneous flowfield is key to developing improved turbulence models for accurate prediction.[6–9]

An example of a canonical two-dimensional (2D) SBLI flowfield is shown in figure 1, where an incident oblique shock impinges on a turbulent boundary layer. Depending on the strength of the impinging shock, the flow in the interaction region may be attached, incipiently separated, or fully separated, the last of these is shown in figure 1. The streamwise length of the separation is L_{sep}. The development of the separation results in the forward migration of the reflected shock. The interaction length, obtained by extending the inviscid portions of the incident and reflected shocks to the wall, is L_{int}. The growth and collapse of

separation causes the reflected shock to oscillate aft (collapse phase) and forward (growth phase) with a characteristic low frequency. Numerous experimental and computational works have shown the Strouhal (frequency) number (St) to lie between $0.01 - 0.05$,[10] where $St = fL_{int}/\overline{u}_\infty$. This spread in frequency is related to the length of the separation; larger separation length leads to longer period of growth and collapse cycle, thus resulting in lower characteristic frequency of the reflected shock and vice versa. Importantly, the underlying physics remain the same across a multitude of impinging shock strengths, but variations in flow topology are present due to the size and shape of the separation.[11]
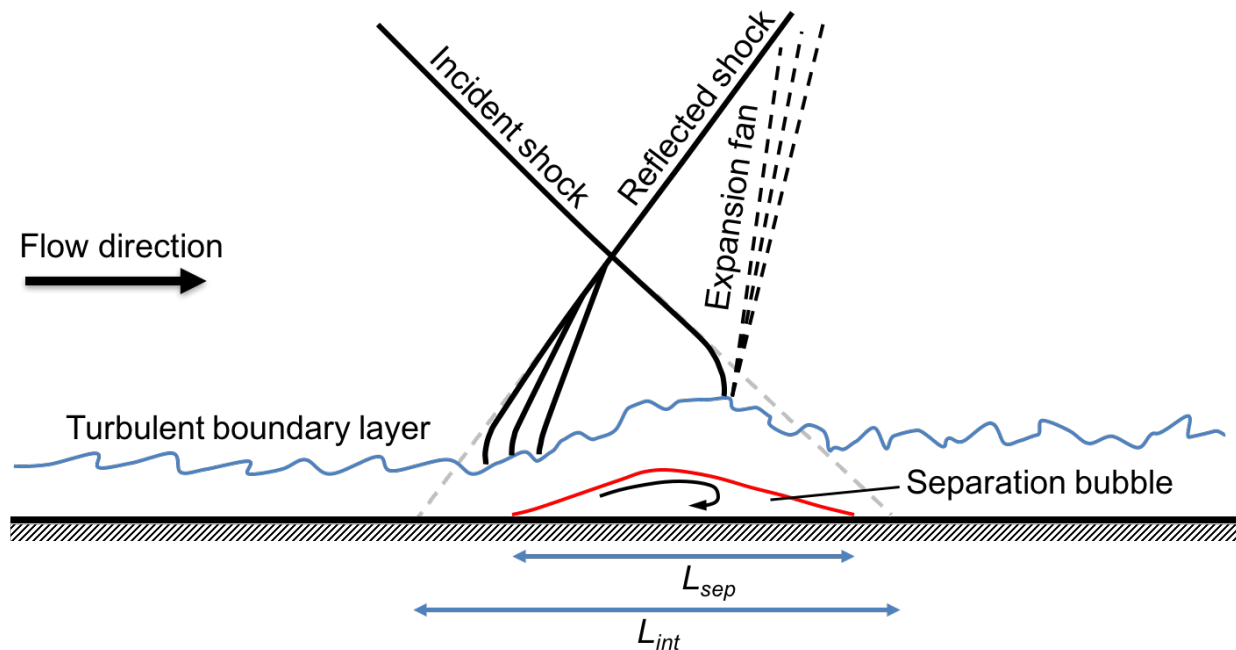

Figure 1. Two-dimensional anatomy of an impinging shock wave/boundary-layer interaction.

In most practical applications, Reynolds-averaged Navier-Stokes (RANS) computational fluid dynamics (CFD) solvers coupled with turbulence models are used to calculate flowfields where SBLIs are present. This is mainly due to their ease of use, and also because of the challenges presented by scale-resolving methods like hybrid RANS/large-eddy simulations (LES), LES, and direct numerical simulations (DNS) in the form of available computer resources and lengthy simulation times. However, scale-resolving methods can offer significant gains in accuracy.

A list of scale-resolving approaches is compiled by Georgiadis et al.[12] in a paper that provides a summary of current practices in LES. In LES, large-scale structures are resolved and a subgrid-scale model is employed to model the scales which cannot be resolved by the mesh. A subset of LES is implicit LES (ILES). Like LES, ILES calculates the large-scale turbulent structures, but it does not explicitly model the smallest scales. High-order finite difference schemes are used to calculate the spatial derivatives. Thus, numerical dissipation is not provided implicitly by the discretization scheme. This is accomplished by a high-order low-pass Padé-type filter to dissipate energy in the high spatial wavenumber range.[13,14] Thus providing an implicit sub-grid closure.[15] Therefore, ILES combined with a wall-resolved mesh is an attractive approach (also known as wall-resolved LES) for this work as it is not as expensive as DNS, but does provide a seamless changeover to DNS as the mesh resolution is refined.

In the authors' previous work, terms in the exact equation of turbulent kinetic energy (TKE) were studied for a developing turbulent boundary layer and an SBLI.[16] However, due to increased interest in Reynolds-stress models, here the focus is shifted on the exact equation of Reynolds-stress transport. Understanding of the various terms in the exact equation and their interactions with each other would shed light on the fundamental mechanisms present in SBLI. This knowledge may be used to improve the current turbulence models and/or propose new models. In the past, such efforts involved DNS studies of turbulent boundary layers,[6] channel flows,[9] and square ducts.[7] Recently, Schiavo et al.[17] studied TKE and Reynolds-stress

budgets in a channel flow with a 2D bump to examine the effects of an adverse pressure gradient. Relevant to the present work, Pirozzoli and Bernardini[18] performed a DNS of an impinging SBLI at $Re_\theta = 2300$ and calculated the TKE budgets. Morgan et al.[19] also computed TKE budgets at several Re_θ for the same flow conditions, but further showed a limited comparison of the $\overline{\rho u'' u''}$ and $\overline{\rho v'' v''}$ budgets with that of Wilcox Stress-ω.[20] In the work preceding this paper,[21] the authors provided the first comprehensive examination of the Reynolds-stress transport terms within a quasi-two-dimensional SBLI flowfield. In this paper, the computational domain is expanded to include the sidewalls, which render the flowfield three-dimensional due to the ensuing corner separation. As previously mentioned, such a flow topology is common in inlets and isolators of supersonic aircraft and thus critically important. Our objective is twofold:

- Validate the simulation with the experimental database to ensure consistency of the computed quantities.

- Study the budgets of Reynolds stress and other relevant turbulence quantities with an intent to inform future model development.

II. Governing Equations

In this section the Reynolds stress transport equation will be discussed along with the equations pertinent to the ILES formulation and the digital filter approach, which is used to obtain turbulent fluctuations at the inflow.

II.A. Reynolds-stress Budget

The Reynolds stress is defined as:

$$\bar{\rho}\tau_{ij} = -\overline{\rho u_i'' u_j''} \tag{1}$$

and its transport is given by equation 2.[20]

$$\frac{\partial}{\partial t}\left(\overline{\rho u_i'' u_j''}\right) + \frac{\partial}{\partial x_k}\left(\overline{\rho u_i'' u_j''}\tilde{u}_k\right) = \mathcal{P}_{ij} + \mathcal{D}_{ij} + \Pi_{ij} - \bar{\rho}\epsilon_{ij} + \mathcal{M}_{ij} \tag{2}$$

The first term on the left-hand side represents the unsteady term, while the second term represents the convection—together, the left-hand side is the substantial derivative. The budget terms are on the right-hand side, and defined as:

$$\mathcal{P}_{ij} = -\overline{\rho u_i'' u_k''}\frac{\partial \tilde{u}_j}{\partial x_k} - \overline{\rho u_j'' u_k''}\frac{\partial \tilde{u}_i}{\partial x_k} \qquad \text{Production} \tag{3}$$

$$\mathcal{D}_{ij} = \mathcal{D}_{ij}^{\nu} + \mathcal{D}_{ij}^{T} + \mathcal{D}_{ij}^{P} \qquad \text{Diffusion} \tag{4}$$

$$\mathcal{D}_{ij}^{\nu} = \frac{\partial}{\partial x_k}\left[\overline{u_i'' t_{kj} + u_j'' t_{ki}}\right] \qquad \text{Molecular Diffusion} \tag{5}$$

$$\mathcal{D}_{ij}^{T} = -\frac{\partial}{\partial x_k}\left[\overline{\rho u_i'' u_j'' u_k''}\right] \qquad \text{Turbulent Diffusion} \tag{6}$$

$$\mathcal{D}_{ij}^{P} = -\frac{\partial}{\partial x_k}\left[\overline{p' u_i''}\delta_{jk} + \overline{p' u_j''}\delta_{ik}\right] \qquad \text{Pressure Diffusion} \tag{7}$$

$$\Pi_{ij} = \overline{p'\left(\frac{\partial u_i''}{\partial x_j} + \frac{\partial u_j''}{\partial x_i}\right)} \qquad \text{Pressure Strain} \tag{8}$$

$$\bar{\rho}\epsilon_{ij} = \overline{t_{ki}\frac{\partial u_j''}{\partial x_k}} + \overline{t_{kj}\frac{\partial u_i''}{\partial x_k}} \qquad \text{Dissipation} \tag{9}$$

$$\mathcal{M}_{ij} = \overline{u_i''}\left(\frac{\partial \bar{t}_{kj}}{\partial x_k} - \frac{\partial \bar{p}}{\partial x_j}\right) + \overline{u_j''}\left(\frac{\partial \bar{t}_{ki}}{\partial x_k} - \frac{\partial \bar{p}}{\partial x_i}\right) \qquad \text{Turbulent Mass Flux} \tag{10}$$

Here t_{ij} is the viscous stress tensor based on the instantaneous strain-rate tensor s_{ij}, and δ_{ij} is the Kronecker delta.

$$t_{ij} = 2\mu s_{ij} + \zeta \frac{\partial u_k}{\partial x_k} \delta_{ij} \tag{11}$$

In equation 11, ζ is obtained by relating it to μ. Such an assumption is valid for monatomic gases and widely used in computational fluid dynamics.

$$\zeta = -\frac{2}{3}\mu \tag{12}$$

II.B.   Compressible Navier-Stokes Equations

The compressible Navier-Stokes equations in non-dimensional form are given by

$$\frac{\partial \rho}{\partial t} + \frac{\partial}{\partial x_i}(\rho u_i) = 0 \tag{13}$$

$$\frac{\partial}{\partial t}(\rho u_i) + \frac{\partial}{\partial x_j}\left(\rho u_i u_j + p\delta_{ij} - \frac{1}{Re}t_{ij}\right) = 0 \tag{14}$$

$$\frac{\partial}{\partial t}(\rho e_0) + \frac{\partial}{\partial x_i}\left[u_i(\rho e_0 + p) - \frac{1}{Re}(u_j t_{ij}) + \frac{1}{(\gamma-1)PrM^2Re}q_i\right] = 0 \tag{15}$$

The total energy and heat flux are defined as

$$e_0 = e + \frac{1}{2}u_i u_i \qquad\qquad q_i = -\mu\frac{\partial T}{\partial x_i} \tag{16}$$

The non-dimensionalization is performed using the following definitions where * (asterisk) represents non-dimensional quantities. Except for equations 17a and 17b, the * has been dropped for simplicity and all quantities are non-dimensional in this paper, unless stated otherwise.

$$x_i^* = \frac{x_i}{L} \qquad u_i^* = \frac{u_i}{V_{ref}} \qquad t^* = \frac{tV_{ref}}{L} \qquad \rho^* = \frac{\rho}{\rho_{ref}} \tag{17a}$$

$$p^* = \frac{p}{\rho_{ref}V_{ref}^2} \qquad T^* = \frac{T}{T_{ref}} \qquad \mu^* = \frac{\mu}{\mu_{ref}} \qquad e^* = \frac{e}{V_{ref}^2} \tag{17b}$$

The reference conditions are the upstream freestream conditions and the length scale, L, is the upstream boundary-layer thickness, both are discussed later in section III.B. The non-dimensional parameters Reynolds number, Prandtl number, and Mach number are defined below. The specific heat at constant pressure is C_p and κ_{ref} is the thermal conductivity constant. The molecular viscosity, μ_{ref}, is calculated using Sutherland's law at the reference temperature and a perfect gas is assumed.

$$Re = \frac{\rho_{ref}V_{ref}L}{\mu_{ref}} \qquad Pr = \frac{\mu_{ref}C_p}{\kappa_{ref}} \qquad M = \frac{V_{ref}}{\sqrt{\frac{\gamma p_{ref}}{\rho_{ref}}}} \tag{18}$$

The above Navier-Stokes equations can be expressed in flux-vector form, transformed into curvilinear coordinates, and written in the strong conservation form.[22,23]

II.C.   Unsteady Inflow Boundary Method

In an effort to facilitate generation of turbulent boundary layer, a robust and computationally inexpensive method was sought. Based on our past experience of using the digital filter approach,[21] for a periodic SBLI simulation, the same approach was used here. Modifications were made to extend the digital filter to include the two sidewalls as well.

II.C.1. The Digital Filter Approach

The digital filter approach was originally proposed by Klein et al.,[24] where the filtering operation was performed in 3D space. Later, Veloudis et al.[25] investigated specification of varying filter coefficients in the wall-normal direction to allow for varying length scales. Xie and Castro[26] simplified and sped up the approach by performing the filtering operation on the 2D inflow plane and correlating the calculated 2D field with the one at the previous timestep to account for the length scale in the streamwise direction using Taylor's hypothesis.[27] The approach was further improved by Touber and Sandham[28] and the current work closely follows their implementation of the digital filter.

Detailed numerics of the method were described in Vyas et al.[21] and hence omitted here. In general, the following steps are taken within the digital filter algorithm:

1. Generate a set of p random numbers with zero mean and unit variance corresponding to the 2D inflow mesh. Here, the Box-Muller theorem is used to combine two independent and uniformly distributed sets of numbers a and b in the range $(0, 1)$ into c and d, which are independent and normally distributed, and also satisfy zero mean and unit variance conditions. They can be calculated as below, however, either one can be used.

$$c = \sqrt{-2\ln(a)}\cos(2\pi b) \qquad\qquad d = \sqrt{-2\ln(a)}\sin(2\pi b) \qquad (19)$$

2. Select the relevant turbulence length scales, I_x, I_y, and I_z. Since the current implementation is 2D, I_y and I_z are converted into an equivalent number of grid points using a grid spacing, i.e., $n_\alpha = I_\alpha/\Delta\alpha$. The choice of grid spacing is critical, small values will lead to large filter width and impose nonphysical correlation. Computationally, it will slow down the digital filter. In contrast, when Δy and Δz are large, the filter would become narrow and thus cutoff the influence of significant neighboring fluctuations, resulting in delayed recovery of expected velocity and Reynolds stress profiles. Consequently, a grid spacing in log-law region was picked based on a limited sensitivity study, but the results of the study are not shown here.

3. Now the filter coefficients can be calculated using the equation below, where the filter bounds are $N_\alpha = 2n_\alpha$.

$$b_{jk} = \frac{\exp\left[-\pi\left(\dfrac{|j|}{n_y} + \dfrac{|k|}{n_z}\right)\right]}{\left\{\displaystyle\sum_{k=-N_z}^{N_z}\sum_{j=-N_y}^{N_y}\exp\left[-2\pi\left(\dfrac{|j|}{n_y} + \dfrac{|k|}{n_z}\right)\right]\right\}^{1/2}} \qquad (20)$$

4. The filter coefficients calculated in equation 20 can now be used to filter the zero mean and unit variance normally distributed random numbers calculated in equation 19. Thus, we impose relevant $y - z$ length scales on the field of these normally distributed random numbers using equation 21.

$$v_{mn} = \sum_{j=-N_y}^{N_y}\sum_{k=-N_z}^{N_z} b_{jk} r_{(m+j)(n+k)} \qquad (21)$$

5. The length scale in the x direction is imposed by correlating the old time step $(t - \Delta t)$ to the current time step (t). This 2D filtering process was demonstrated by Xie and Castro[26] in contrast to the 3D filtering originally proposed by Klein et al.[24] In equation 22, Δt is the time step, t_L is the Lagrangian time scale, such that $t_L = I_x/\bar{u}_{RANS}$, and $\mathbf{v}_{mn}$ is the complete fluctuation that has all three length scales built into it.

$$\mathbf{v}_{mn}^t = \mathbf{v}_{mn}^{t-\Delta t}\exp\left(-\frac{\pi\Delta t}{2t_L}\right) + v_{mn}^t\sqrt{1 - \exp\left(-\frac{\pi\Delta t}{t_L}\right)} \qquad (22)$$

6. The final step involves the transformation originally proposed by Lund et al.[29] to obtain a time-dependent inflow velocity field. Components of a_{ij} are defined by the Reynolds-stress tensor (τ_{ij}).

Both, $\overline{u}_i$ and τ_{ij} are obtained from a previous RANS turbulent flat plate calculation performed on the same mesh as the LES simulation, at identical Mach and Reynolds numbers, using the $k - \epsilon$ turbulence model as described in Gerolymos.[30] Grid indices (m, n) used above are removed from equation 23 to write it in compact indicial notation.

$$u_i = \overline{u}_i + a_{ij}\mathbf{v}_j^t \tag{23}$$

$$a_{ij} = \begin{bmatrix} \sqrt{\tau_{11}} & 0 & 0 \\ \tau_{21}/a_{11} & \sqrt{\tau_{22} - a_{21}^2} & 0 \\ \tau_{31}/a_{11} & (\tau_{32} - a_{21}a_{31})/a_{22} & \sqrt{\tau_{33} - a_{31}^2 - a_{32}^2} \end{bmatrix} \tag{24}$$

7. Lastly, the calculation of thermodynamic fluctuations was addressed by Touber and Sandham[28] by invoking the Strong Reynolds Analogy (SRA). However, they noted that the validity of such an assumption is debatable, since it holds true in a weak sense as shown by Guarini et al.[31] in a DNS simulation of Mach 2.5 supersonic turbulent boundary layer. Since the goal here is to provide an approximate first guess at the inflow plane, this approach was determined to be sufficient and is shown below:

$$\frac{T'}{\overline{T}} = -(\gamma - 1)M^2\frac{u'}{\overline{u}} \qquad \text{where} \qquad M^2 = \frac{\overline{\rho}\overline{T}}{\gamma\overline{p}} \tag{25}$$

8. Invoking SRA also means that the pressure fluctuations in the boundary layer are negligible, i.e., $p' = 0$. Thus, the following relation for the density fluctuations results:

$$\frac{\rho'}{\overline{\rho}} = -\frac{T'}{\overline{T}} \tag{26}$$

This concludes the procedure that generated the time-dependent fluctuating inflow plane. The filter parameters are provided in table 1.

Table 1. Digital filter parameters

Parameter	x	y	z
Length Scale, I_α [a]	0.5	0.25	0.25
$\Delta\alpha$ [b]	-	0.01	0.01
Equivalent Gridpoints, $N_\alpha = 2I_\alpha/\Delta\alpha$	-	50	50

[a] Non-dimensionalized by δ_{99}
[b] $\alpha = y, z$

III. Simulation Methodology

III.A. Numerical Schemes

The sixth-order compact spectral-like finite-difference scheme of Lele,[32] adapted by Visbal and Gaitonde,[33] was implemented in the FDL3DI code to calculate spatial derivatives. An eighth-order low-pass Padé-type non-dispersive spatial filter is applied after each sub-iteration to maintain stability and dissipate energy in the high spatial wavenumber range where the turbulent energy spectrum is poorly resolved.[13, 14] The filter coefficient, α_f, which determines sharpness of the filter cutoff was set to 0.475. The highest possible filter coefficient was desired since that results in the lowest amount of numerical dissipation introduced in the simulation, thus providing an accurate physical dissipation. But this needs to be moderated with possible stability issues in a complex SBLI investigation performed in this work. Shock capturing was performed using a hybrid compact-Roe approach of Visbal and Gaitonde,[34] where the smoothness criterion, adopted from the weighted essentially non-oscillatory (WENO) scheme,[35] was used to detect the shock. The threshold

parameter (ϵ) was specified to be 1×10^{-9} and the shock sensor exponent (n) was chosen to be 2.2. Once the shock was identified the spatial filter was turned off and the numerical scheme was switched to third-order Roe with the van Leer harmonic limiter.[36] The implicit time integration was performed with the second-order Beam-Warming[37] scheme using two Newton-like sub-iterations and approximate factorization. The non-dimensional time step based on the reference conditions (table 2) for this problem was 0.002.

Since the primary intent of this work is to study the budget of the exact Reynolds-stress transport, the above method allowed forgoing an explicit subgrid-scale model. Such an approach was taken by Morgan et al.,[19] where flow conditions similar to the present study were used for $Re_\theta = 4800$ and comparisons were made with the DNS of Pirozzoli and Bernardini[18] which showed that at low to moderate Reynolds number, omitting an explicit subgrid-scale model is suitable. Kawai et al.[38] showed that inclusion of an explicit subgrid-scale model in addition to the low-pass filtering introduced excessive numerical dissipation of the resolved turbulence, which may underpredict turbulence statistics sought here. A comparison of high-fidelity implicit and sub-grid scale model LES for airfoils at low Reynolds number performed by Garmann et al.[39] showed no benefit in using an explicit subgrid-scale model. Thus, high-fidelity ILES is an attractive approach for this work as it is paired with wall-resolved meshes.

III.B.   Boundary Conditions and Mesh Parameters

The flow conditions represent the experiments[4] performed at the Institut Universitaire des Systèmes Thermiques Industriel (IUSTI) in Marseille, France for an 8° deflection angle. Table 2 shows a comparison of experimental and simulated flow conditions.

Table 2.   8.0-degree deflection angle: Centerline flow conditions upstream of the interaction region at $(x - x_{imp}) = -5.7$

Property	Experiment	Simulation (nominal)
M_∞	2.29	2.29
U_∞, m/s	545.0	545.0
P_∞, Pa	50663	50663
T_0, K	300	300
δ_{99}, mm	10.0	11.0
θ, mm	0.87	0.88
δ^*, mm	3.0	3.1
Re_δ	53420	54000
Re_θ	4640	4600

The computational domain for the simulation focuses on the SBLI region. At the inflow of the computational domain, digital filtering was used to generate unsteady fluctuations and provide a turbulent boundary layer. The walls were treated as no-slip and adiabatic. Figure 2(a) shows a comparison of the precursor half-span RANS simulation and corresponding WRLES domain, although the WRLES simulation was full span. A portion of the farfield boundary, which extended from the inflow to $x = -0.36$, was obtained from the RANS solution to impose the three-dimensional impinging shock. Downstream of the RANS-derived farfield boundary condition, extrapolation was used. Extrapolation was also used at the outflow boundary. Mesh topology is shown in figure 2(b) for the region of interest where the coordinates are non-dimensionalized by the length scale δ_{99}. For the purpose of clarity, only every fourth and eighth points are shown in x- and y-directions, respectively. In this region a constant x-spacing was maintained. Hyperbolic tangent grid clustering was maintained at the walls in the y- and z-directions up to δ_{99}, beyond which $\Delta y = \Delta z$ was kept constant. Table 3 shows a list of parameters for various meshes used in a refinement study (periodic simulations) and the final full span mesh.
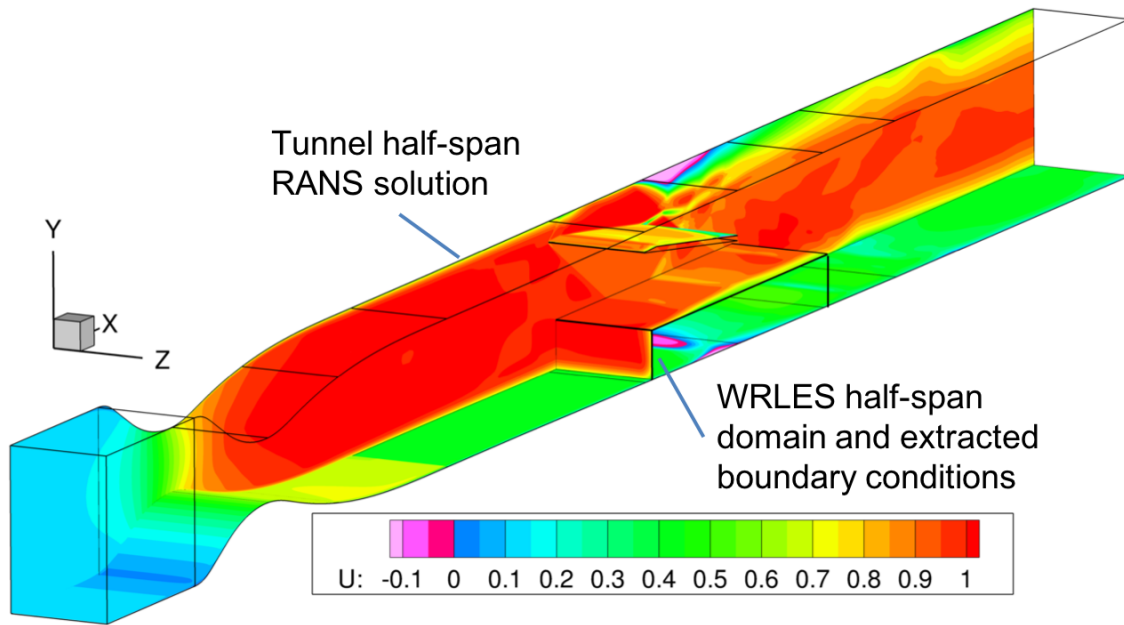
(a) Boundary conditions. Only half-span is shown.
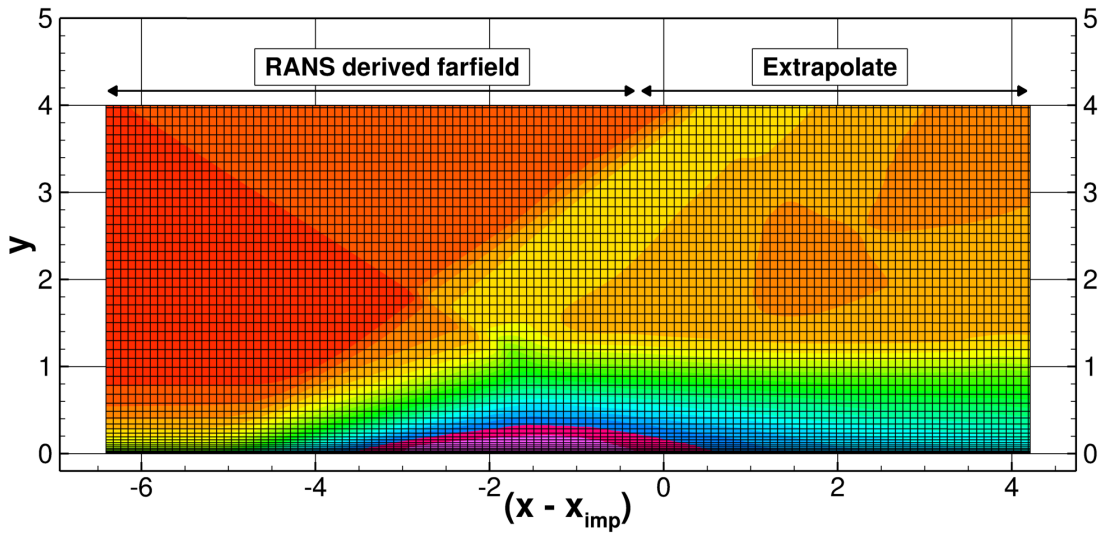
(b) Mesh topology in the region of interest along the centerline. Coordinates non-dimensionalized by the experimental δ_{99}. Every 4th point in the x direction and 8th point in the y direction is shown for clarity.

Figure 2. Boundary conditions and mesh parameters

Table 3. Mesh parameters

	Periodic Simulations				Full-span Simulation
	Baseline	x-Refine	y-Refine	z-Refine	fs-Baseline
Domain size					
$x \times y \times z$[a]	$30 \times 4 \times 5$	$30 \times 4 \times 5$	$30 \times 4 \times 5$	$30 \times 4 \times 5$	$30 \times 4 \times 17$
Computational points					
$N_x \times N_y \times N_z$	$1025 \times 257 \times 257$	$2049 \times 257 \times 257$	$1025 \times 513 \times 257$	$1025 \times 257 \times 513$	$1025 \times 395 \times 1489$
N_{total}	68×10^6	135×10^6	135×10^6	135×10^6	603×10^6
Constant region					
N_x	945	1889	945	945	945
Δx	0.0212	0.0105	0.0212	0.0212	0.0212
At $(x - x_{imp}) = -5.7$					
Δx^+	15	7	15	15	15
$N_{y,bl}$	187	187	344	187	162
Δy_w	1×10^{-3}	1×10^{-3}	1×10^{-3}	1×10^{-3}	1×10^{-3}
Δy_w^+	0.68	0.68	0.68	0.68	0.68
Δz_c^+	13	13	13	7	10
Δz_w	n/a[b]	n/a	n/a	n/a	1×10^{-3}
Δz_w^+	n/a	n/a	n/a	n/a	0.68

[a] x, y, z are non-dimensionalized by δ_{99}

[b] Not applicable

IV.   Results

IV.A.   Comparison with the Experiment

The time-averaged van Driest transformed velocity profiles are presented in figure 3(a) for the upstream undisturbed boundary layer at $(x - x_{imp}) = -5.7$. The baseline, x-Refine, y-Refine, and z-Refine results are the periodic simulations from our previous study[21] and thus span-averaged. The fs-Baseline is the full-span result, consequently, only the centerline profile is shown. The comparison of all simulations illustrate that the streamwise velocity is insensitive to the mesh refinement in the x and y directions. However, the refinement in the z direction shows a clear improvement in the logarithmic law (log-law) region ($\kappa = 0.41$ and $B = 5.5$). The fs-Baseline mesh, which was developed from the above mesh sensitivity study, shows excellent comparison with the laser Doppler anemometry (LDA) and particle image velocimetry (PIV) experimental[40] data. Further, the skin friction profiles for all periodic and full-span cases are presented in figure 3(b). It can be observed that the periodic simulations significantly underpredict the separation region, indicated by the narrow negative skin friction region. Moreover, the baseline, x-Refine, and y-Refine meshes underpredict the skin friction, while the z-Refine mesh overpredicts the skin friction in the upstream undisturbed boundary layer in comparison to the hot-wire anemometry (HWA) data.[41] In contrast, the full-span result shows the best comparison with the experimental data in the upstream undisturbed boundary layer. Also of note is the separation length, even though the region between $(x - x_{imp}) = 0$ to 1.5 seems to have reattached in the experiment, the simulation shows separated flow. This is indicative of a larger overall interaction region. However, downstream of $(x - x_{imp}) = 2.0$ the simulation shows a reattached boundary layer and is in excellent comparison with the experiment.
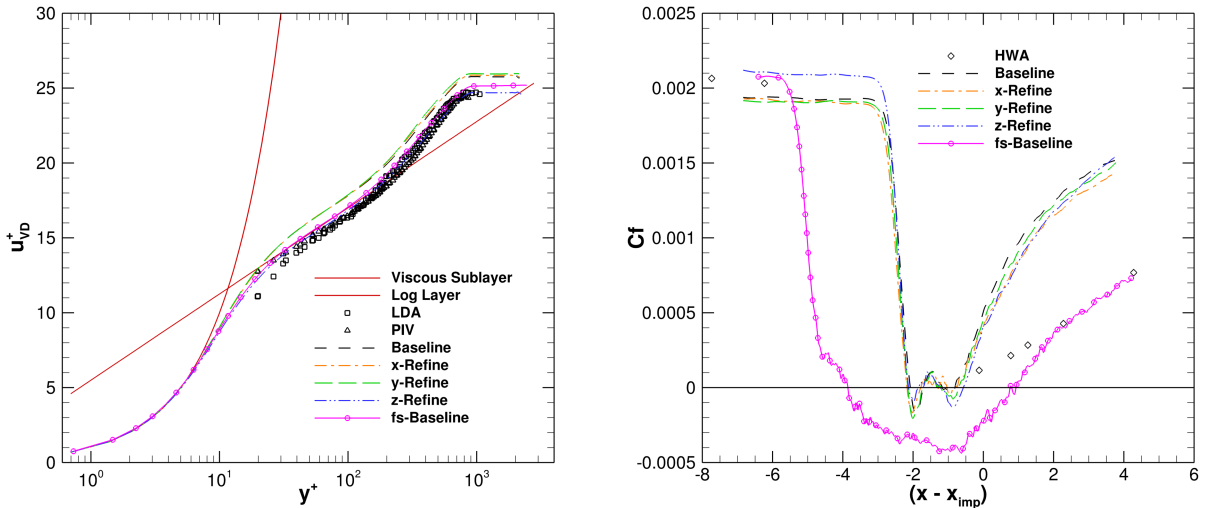
(a) van Driest transformed streamwise velocity profiles at $(x - x_{imp}) = -5.7$

(b) Skin friction coefficient profiles

Figure 3.   Mean flow comparison with the experimental data.

It is a common practice among experimentalists to calculate the interaction length (L_{int}) in an SBLI experiment, since measuring separation length (L_{sep}) is difficult using point probe techniques like pitot measurement and HWA, while field imaging and scattering techniques like PIV and LDA, respectively, often cannot reach to the wall due to reflections. Thus, the interaction length is calculated by virtually extending the inviscid portions of the impinging and reflected shocks to the wall, and measuring the distance between the foot of each shock. Table 4 shows a comparison of the interaction lengths from various periodic simulations and the present work to that of the experiment. It is encouraging that the implicit LES, wall-resolved LES, and DNS periodic simulations are remarkably close, but all underpredict the interaction length—an artifact of the periodic boundary condition. Interaction length from the current full-span result confirms that the corner separations plays a key role in amplifying the interaction length along the centerline of the domain. This is especially true for small aspect ratio wind tunnels as shown by Babinsky et al.[42] experimentally in terms of the separation length. However, the argument holds for interaction length as well. Lastly, a word

on the two periodic simulations by Touber and Sandham[28] and Agostini et al.[43] Since these simulations are conventional LES, subgrid-scale models were used and hence the predicted interaction region depends on the choice of these models. Such a behavior has also been observed in RANS, where the interaction region has been shown to vary in size with the choice of turbulence model.[44]

Table 4. Comparison of previous and present simulations with the experimental data

Authors	Nominal Re_θ	Interaction Length[a]	Simulation
Experiment[4]	4600	4.60	-
Touber and Sandham[28]	4600	4.80	Periodic/LES-SGS
Agostini et al.[43]	4600	3.45	Periodic/LES-SGS
Morgan et al.[19]	4800	2.90	Periodic/ILES
Morgan et al.[19]	2300	2.90	Periodic/ILES
Pirozzoli and Bernardini[18]	2300	2.89	Periodic/DNS
Vyas et al.[21]	4600	2.94[b]	Periodic/WRLES
Present work	**4600**	**5.2**	**Full-span/WRLES**

[a] Non-dimensionalized by δ_{99}, i.e., L_{int}/δ_{99}

[b] z-Refine mesh interaction length

In order to understand the key flow features and mechanisms, a comparison of the mean solution in the left half and instantaneous solution in the right half of the flowfield is presented in figure 4. In the mean solution, contours of streamwise velocity at the $y = 0.1$ ($y = 1$ mm) plane with streamlines indicate a large region of separated flow in the center of the domain. Especially at the centerline, the streamlines shift up and around the separation region. The flow is also separated along the corner and stretches forward of the separation along the centerline. In between the centerline and corner separations, there is a region of attached but low-momentum flow, which accelerates aft of the separated flow regions. An isosurface of pressure gradient magnitude was used to represent the mean shock. It can be observed that the shock spans from the centerline up to two-thirds extent in the z direction and begins to breakup as it encounters the sidewall boundary layer. However, the effects of pressure gradient persist. Volume ribbons along the sidewall and streamlines in the corner show a highly three-dimensional flow topology. At the end plane of the sampled data a vortical secondary flow feature can be observed in the corner. Another much smaller, but counter-rotating vortex was also present, but hard to see due to its size. The instantaneous solution in figure 4 was picked so that the reflected shock position approximately matched that of the mean shock, but in reality, it translates fore and aft due to growth and collapse of the separation. Also of note is the forward warping in the impinging shock as it approaches the sidewall, which was a result of the low-momentum flow along the sidewall. Although it is not visible, the forward warping is also present in the reflected shock due to the corner separation. The rendering of a Q-criterion isosurface, colored by streamwise velocity, is also plotted to highlight the separated flow along the bottom and side (obscured by the Q-criterion isosurface) walls. Thickening of the boundary layer along both walls is apparent.

Now comparisons of the $x - y$ plane, along the centerline, with the experiment and associated error are presented in figures 5 to 9 for mean velocities and Reynolds stresses. Prediction from the current simulation shown here was interpolated on to the experimental grid. The interpolated data was also used to calculate the local error magnitude in the same manner as DeBonis et al.[45] and shown in equation 27. Thus, providing an error map based on each experimental $i - j$ location.

$$e(f)_{(i,j)} = \left| (f_{SIM})_{(i,j)} - (f_{EXP})_{(i,j)} \right| \tag{27}$$

In examining figure 5, it is clear that the predicted interaction length is larger than the experiment, approximately by $0.6\delta_{99}$. However, the predicted separation length is larger by $1.5\delta_{99}$. We also know from the literature that for fully separated flows the near-wall excursions of the reflected-shock foot strongly correlates with the size of separation.[4,5] And, since the inviscid shock characteristics are closer to the experiment (less error in $L_{int,sim}$ versus $L_{sep,sim}$), this indicates that the discrepancy should be associated with local separation dynamics. The error in streamwise velocity is concentrated at the foot of the reflected shock and along the band that wraps around the separated flow region. While the error in wall-normal velocity, figure 6, is much smaller, but also peaks in the vicinity of the reflected-shock foot.
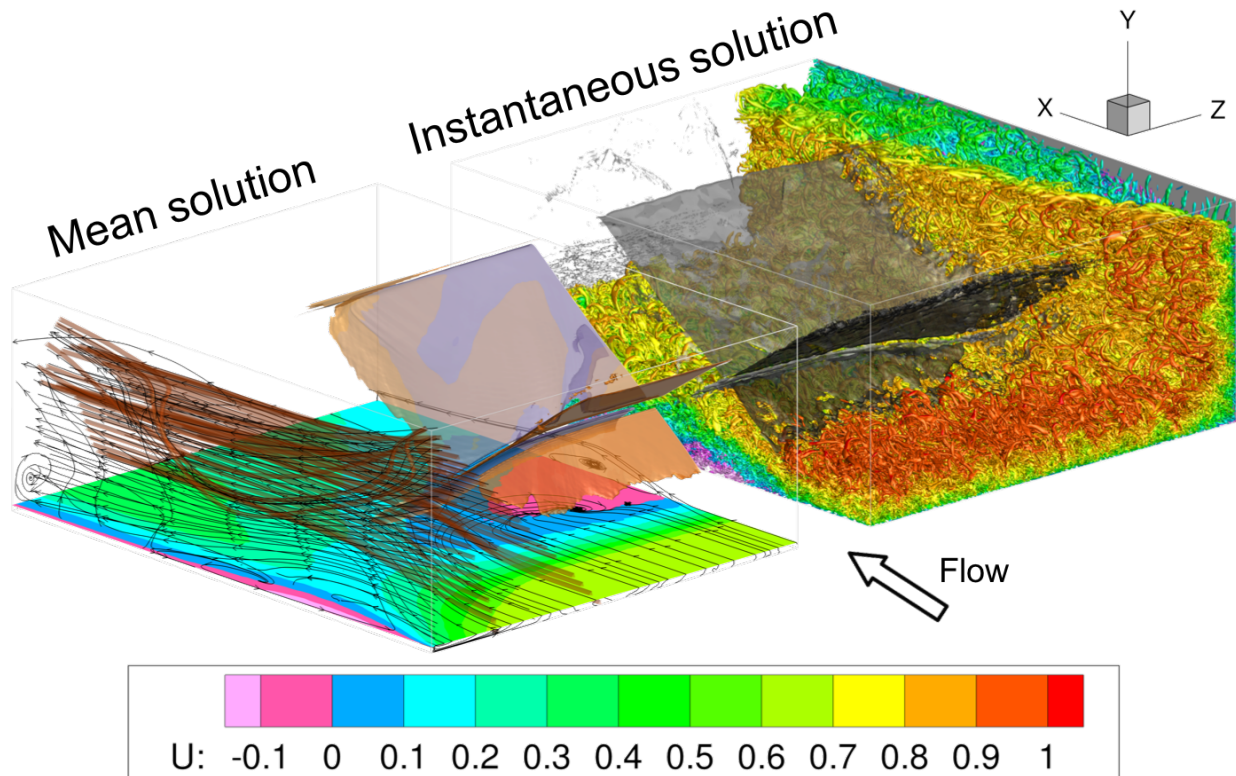
Figure 4. Comparison of the mean solution (left) and instantaneous solution (right). Mean solution: contours of velocity at the $y = 0.1$ ($y = 1$ mm) plane with streamlines showing large 3D separation, secondary flow in the corner, and mean shock position. Instantaneous solution: isosurface of Q-criterion ($Q = 0.5$) colored by velocity showing eddies in the turbulent boundary layer along the bottom wall and the corner.

Investigating the Reynolds stresses in a similar manner sheds more light on the separation and reflected shock codependence, especially regarding the role that upstream influence plays. Figure 7 shows streamwise normal stress ($\sqrt{\overline{u'u'}}$) and the error. While the largest error remained local to the band that wraps around the separated flow, there is non-negligible error in the outer portion of the upstream boundary layer. This results in a smaller $\sqrt{\overline{u'u'}}$, which would make the boundary layer prone to larger separation. In contrast, $\sqrt{\overline{v'v'}}$ (figure 8) does not show the same magnitude of discrepancy in the upstream boundary layer. Furthermore, error in $\sqrt{\overline{v'v'}}$ was smaller across the board but, similar to $\sqrt{\overline{u'u'}}$; it was present in the band that wraps around the separated flow. Finally, the shear stress and error, presented in figure 9, show a secondary band of error emanating from the region where the separation exists in the simulation.

In figures 10(a) and 10(b), the root mean square (RMS) of the streamwise and wall-normal stresses are presented along the centerline for various axial locations upstream of and within the interaction region. At the upstream $(x - x_{imp}) = -5.7$ location, comparison with the experimental data is encouraging. However, lower values of $\sqrt{\overline{u'u'}}$ are obvious beyond $y = 0.4$ as the predicted profile diverges from the experimental data. Touber and Sandham[46] showed similar behavior at the upstream location with the use of digital filtering and the same boundary conditions, but for a periodic SBLI. In $\sqrt{\overline{v'v'}}$, an opposite trend can be observed, where the predicted profile shows a better comparison with the experimental data in the outer portion of the boundary layer and overpredict the near-wall peak. Because the interaction region is larger in the simulation, the next two downstream locations $(x - x_{imp}) = -3.7$ and -1.7 show a larger discrepancy in comparison with the experiment for both streamwise and wall-normal stresses. Outside the interaction region and downstream locations of $(x - x_{imp}) = 0.3$ and 2.3, the predicted profiles show a good match to the experiment up to $y = 0.4$, beyond which the comparison deteriorates; pointing to the upstream boundary layer, specifically, the low $\sqrt{\overline{u'u'}}$ outer portion.

The Reynolds shear-stress profiles along the centerline are presented in figure 11 for the same axial locations. Consistent with the RMS of normal stresses, the Reynolds shear stresses shows a remarkable
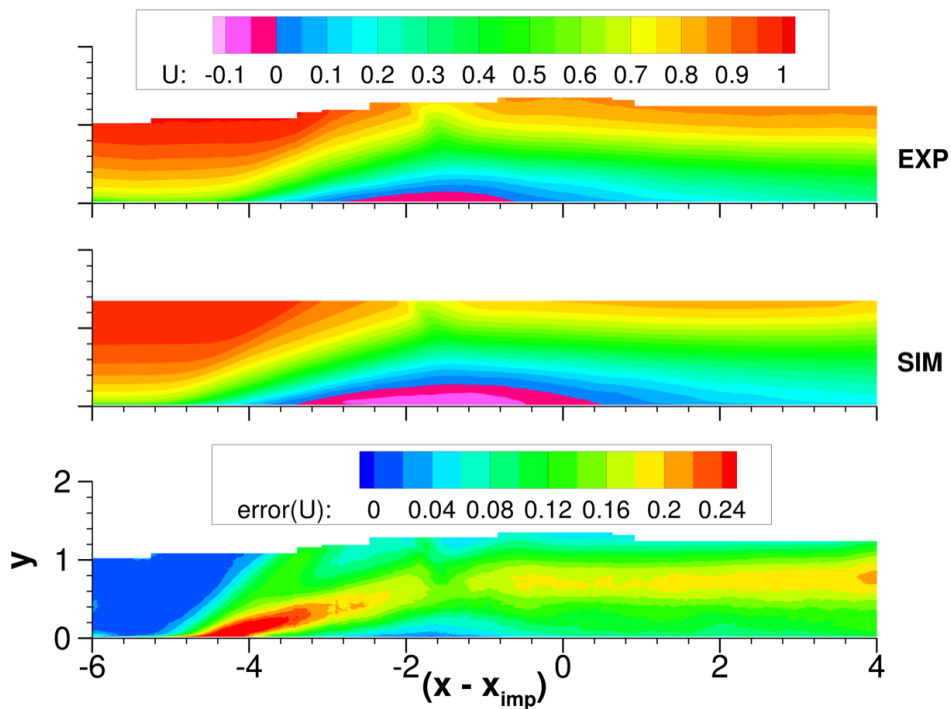
Figure 5. Comparison of the streamwise velocity. Experiment (top), simulation (middle), and associated error (bottom).
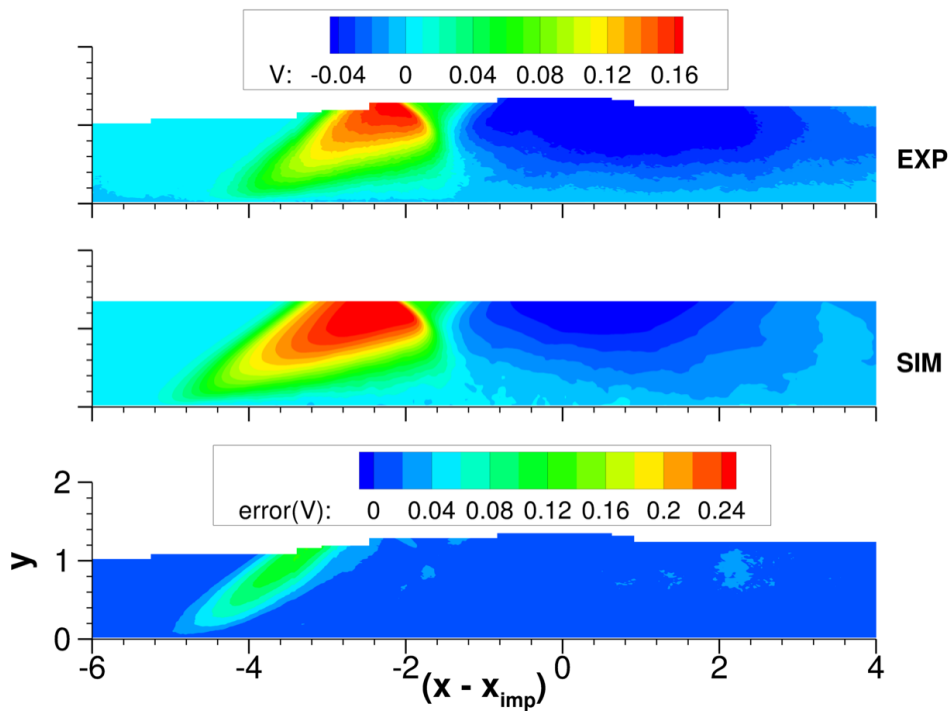

Figure 6. Comparison of the wall-normal velocity. Experiment (top), simulation (middle), and associated error (bottom).

qualitative agreement with the experiment, which is moderated by the fact that the magnitudes at the two locations immediately downstream of the foot of the reflected shock are large and the profiles seem to be shifted outward in the wall-normal direction. This is due to the larger interaction region. Nonetheless, some
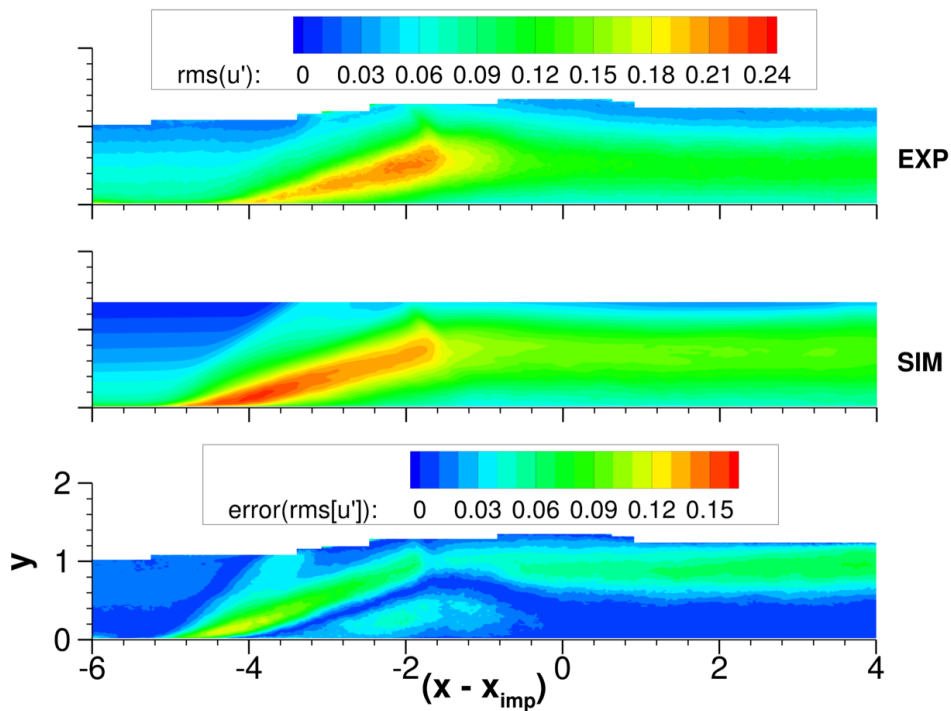
Figure 7. Comparison of $\sqrt{\overline{u'u'}}$. Experiment (top), simulation (middle), and associated error (bottom).
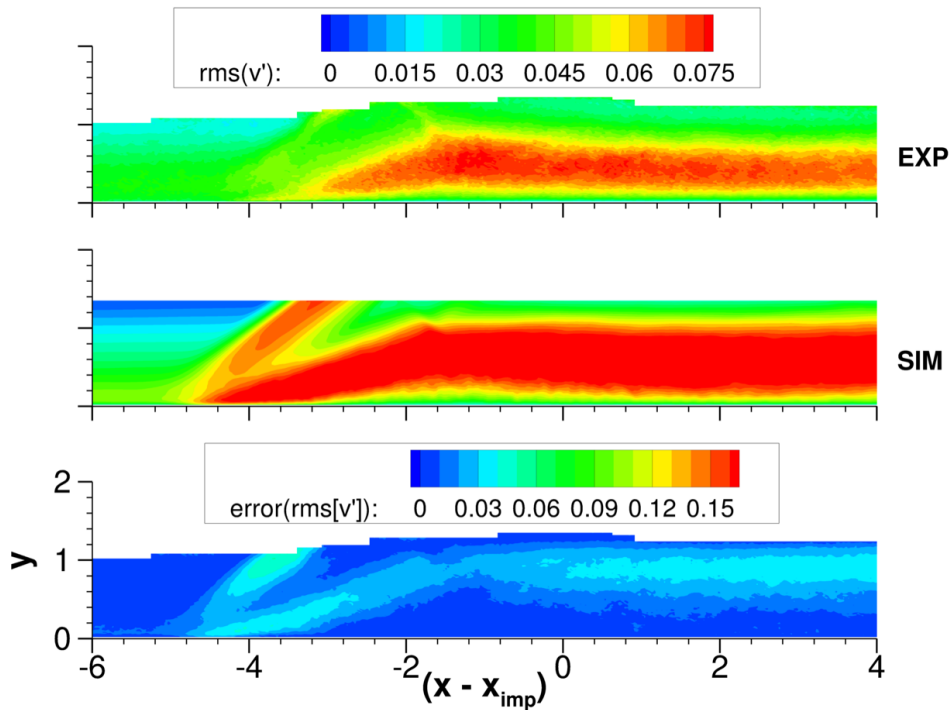
Figure 8. Comparison of $\sqrt{\overline{v'v'}}$. Experiment (top), simulation (middle), and associated error (bottom).

of the key features like increase in the magnitude at $(x - x_{imp}) = -1.7$ and $y = 0.9$, corresponding to the interaction of the impinging shock with the shear layer, was captured. In the near-wall region, a decrease in the magnitude at $(x - x_{imp}) = -3.7$ and $y = 0.15$ is clearly visible.
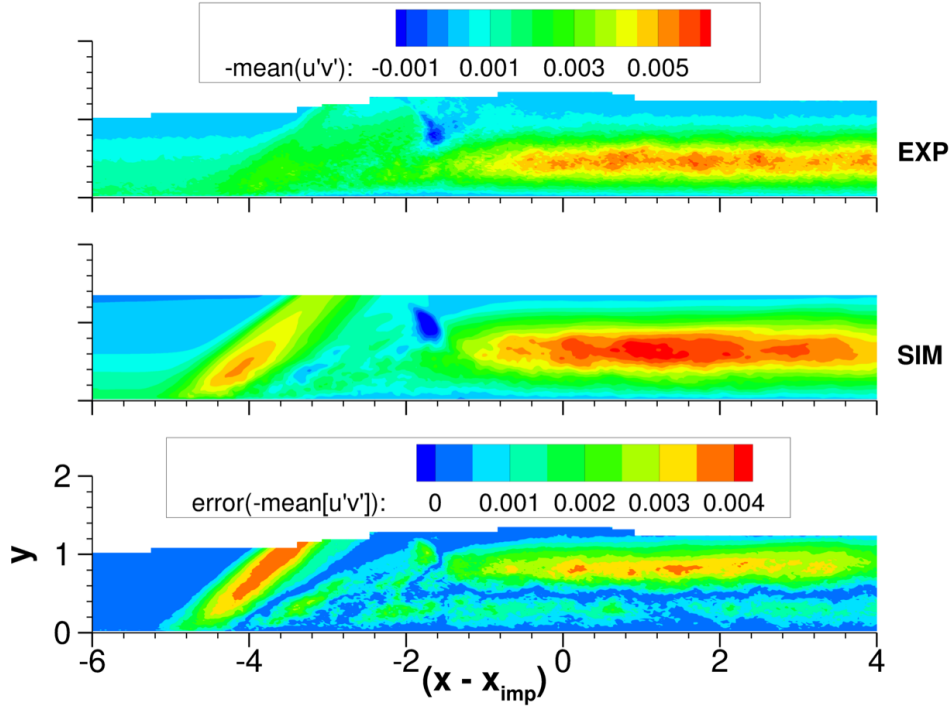
Figure 9. Comparison of $-\overline{u'v'}$. Experiment (top), simulation (middle), and associated error (bottom).

(a) RMS of streamwise stress, $\sqrt{\overline{u'u'}}$

(b) RMS of wall-normal stress, $\sqrt{\overline{v'v'}}$
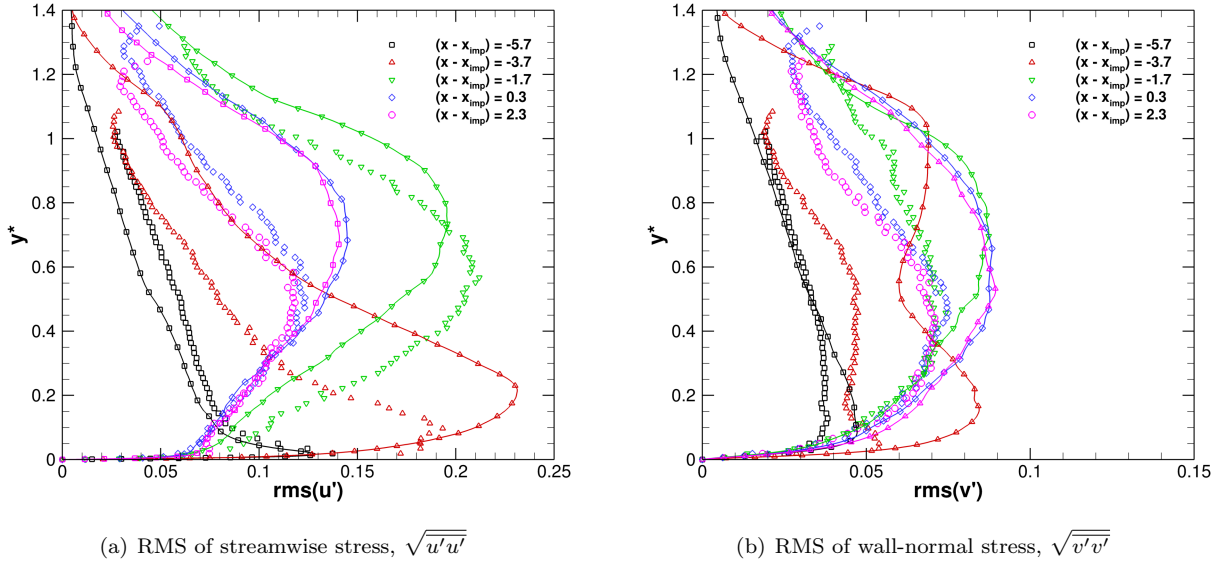
Figure 10. Centerline normal stress RMS profiles at various axial stations. Markers without lines represent experimental data.

IV.B.   Time-series Analysis

Time-series data was acquired at a large number of locations within the volume, which would allow investigation of pressure spectra in various regions of the flowfield. The data was collected for a non-dimensional time period of $1600\delta_{99}/U_\infty$, which corresponds to approximately 10 periods of the separation growth-collapse cycle.

Among these and of particular interest was a rake of six signals located immediately downstream of the reflected shock foot at $(x - x_{imp}) = -4.9$ and extending from the wall to $y = 0.9$ in the wall-normal
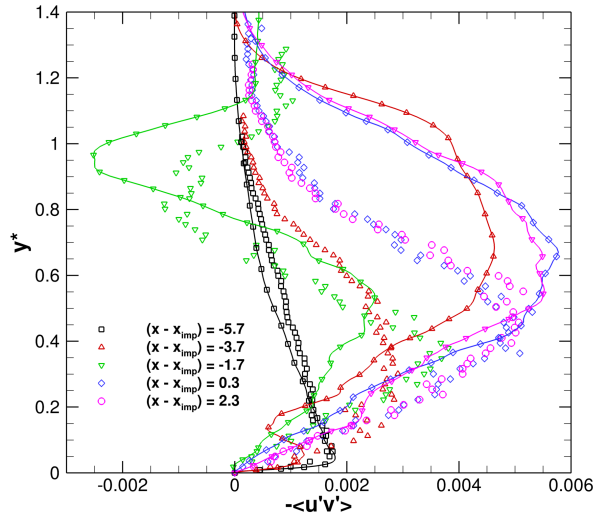
Figure 11. Centerline shear-stress, $-\overline{u'v'}$, profiles at various axial stations. Markers without lines represent experimental data.

direction. Figure 12 shows the weighted power spectral density (PSD) versus the non-dimensional Strouhal number for the six signals compared with the wall signal from the experiment. The weighted PSD was obtained by multiplying the calculated PSD with the frequency and dividing by the integrated PSD over the range of experimental frequencies. The range of frequencies or Strouhal numbers spanned from the lowest to the cutoff frequency of the experiment (50 kHz), which was well within the rate of data acquisition in the simulation (2.7 MHz). This was done to emphasize the Strouhal number associated with the unsteadiness of the reflected-shock foot. While the experimental weighted PSD peaked around $St_{Lint} = 0.03$, the simulation showed the peak around $St_{Lint} = 0.01$. However, this was expected since the simulation shows a larger interaction region, which leads to longer periods of reflected shock foot excursions, which was also noted by Clemens and Narayanaswamy[10] in their review of numerous SBLI literature.

Furthermore, figure 12 shows changing energy in the signals as the foot of the reflected shock passes through the rake. The peak energy in the signal at the wall matches the experiment, however at $y = 0.1$ and 0.2, the energy briefly increases due to their proximity to the shock. The signal at $y = 0.4$ shows an early sign of energy shift in the frequency spectrum with its two peak behavior, where the energy drops to the same level as the wall signal. And at the $y = 0.6$ signal, the energy present at $St_{Lint} = 0.01$ has diminished and shifted to higher frequency at $St_{Lint} = 0.025$. Finally, the peak in energy is completely absent for the signal at $y = 0.9$ since it is sufficiently away from the reflected shock. Thus, the energy is spread across a higher frequency spectrum corresponding to the turbulent boundary layer.
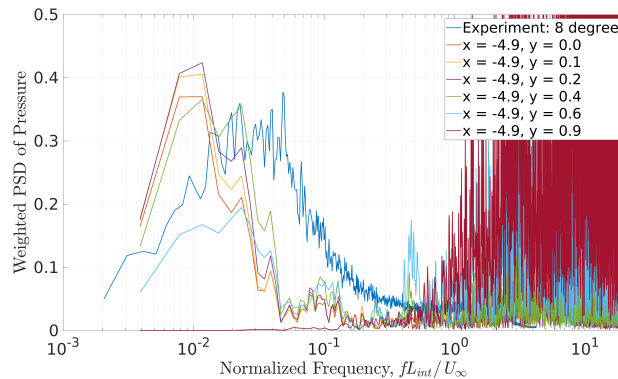

Figure 12. Comparison of the weighted power spectral density with the experiment for the refected-shock foot.

IV.C. Reynolds-stress Budgets

The budget of the Reynolds-stress transport (equations (3) to (10)) was calculated at two axial and three span locations to ascertain effects of the reflected-shock foot and spanwise flow evolution. Figure 13 shows a plane just off the tunnel floor at $y = 0.1$ with these locations (dashed lines). The three span locations also included the corner bisector and the location at $z = 3.7$. The spanwise location of $z = 3.7$, referred to as quarter-span hereinafter, was picked because it is located in the region between the centerline and corner separations. Figure 13 also shows that at $(x - x_{imp}) = -3.7$ the centerline and quarter-span remained attached while the corner is separated.

In past studies, where turbulent boundary layers,[6] channel flows,[9] and square ducts[7] were investigated, the budgets were normalized by $\rho_w u_\tau^4 / \nu_w$. However, doing so would present a problem here since the friction velocity becomes small in the regions of separated flow along the centerline and corners. Thus, in this section, local $\rho_w u_\tau^4 / \nu_w$ at the centerline was used to normalize budgets across the span until $(x - x_{imp}) = -5.7$. Beyond that the centerline $\rho_w u_\tau^4 / \nu_w$ at $(x - x_{imp}) = -5.7$ was used for all downstream locations across the entire span. Similar steps were taken in order to compute the ordinate axis (y^+ or $y^+ = z^+$ for corner bisector).
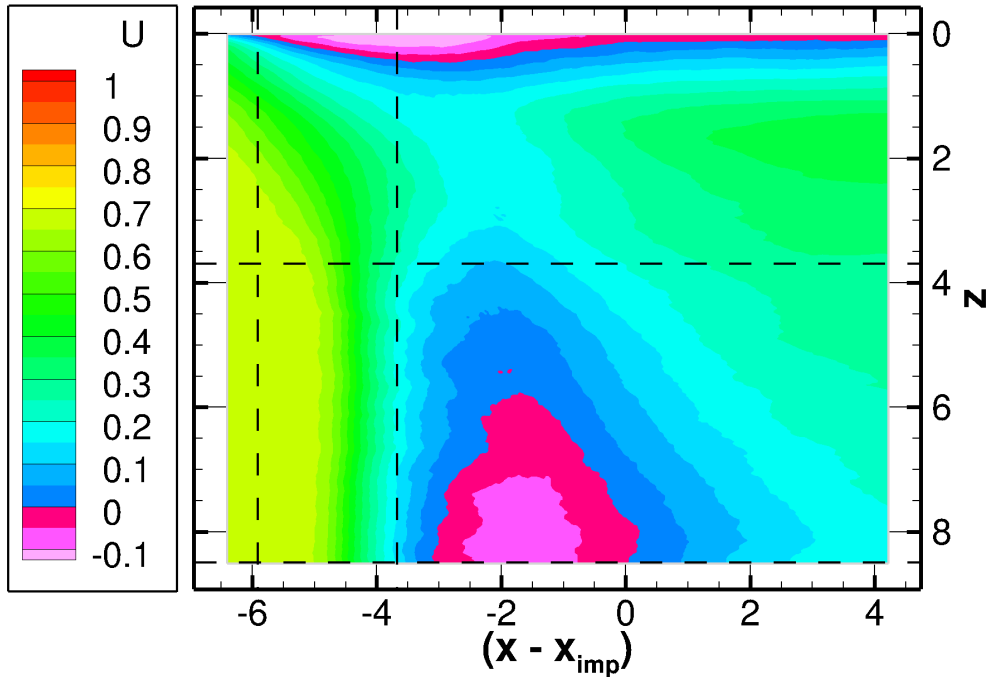
Figure 13. Streamwise velocity at $y = 0.1$ ($y = 1$ mm) plane. Key axial and spanwise locations are marked with the dashed lines.

In addition to the terms in equations (3) to (10), the convective term in equation 2 was also calculated. The sum of the Reynolds-stress budget terms is shown in equation 28. For a steady mean flow, the unsteady term is negligible and the sum should be zero, indicating that the various mechanisms governing the transport of the Reynolds stress are in balance. However, the sum is not expected to remain zero in the SBLI region due to its characteristic unsteadiness. Thus, giving a measure of the unsteady term that was assumed to be zero to calculate the budget sum.

$$\text{Sum} = \mathcal{P}_{ij} + \mathcal{D}_{ij} - \bar{\rho}\epsilon_{ij} + \Pi_{ij} + \mathcal{M}_{ij} - \frac{\partial}{\partial x_k}(\overline{\rho u_i'' u_j''}\tilde{u}_k) = 0 \tag{28}$$

IV.C.1. Effect of the reflected-shock foot: centerline versus corner bisector

In this subsection only the mechanisms responsible for the $\overline{\rho u'' u''}$ budget are presented since the goal here is to highlight the leading trends discovered as of now. Although budgets for other Reynolds stresses were

calculated, more analysis is needed to understand these components and their respective budget mechanisms. Hence they will be discussed in future work.

The budgets of $\overline{\rho u'' u''}$ are shown in figures 14(a) to 14(d). At the upstream centerline (figure 14(a)), the production, molecular and turbulent diffusion, pressure strain, and dissipation terms play a key role, while the pressure diffusion, mass flux, and convective terms remain insignificant. Such a relationship among relevant mechanisms is common in boundary layers and agrees with previous investigations[6,7,9] performed at relatively low Reynolds number. A small error exists in the buffer layer for the sum of all mechanisms (equation 28). Such an error was also observed in the periodic SBLI study,[21] the work that preceded the current paper. Despite the fact that considerable mesh refinement was applied, the error seems to have marginally grown. This suggests a dependence on the extent of the spanwise domain and inclusion of the sidewalls, which led to long convergence periods in obtaining an ensemble average.

In comparing figures 14(a) and 14(c), it is clear that along the centerline, molecular diffusion balances dissipation at the wall and in the viscous sublayer. But along the corner bisector a new behavior in the viscous sublayer emerges, where pressure strain balances molecular diffusion and dissipation. As expected, at the corner origin all quantities are zero. Unlike the centerline, molecular diffusion has a negative contribution to the budget in this region. This can be attributed to the presence of the corner separation and its coupling with the secondary flow. Existence of secondary flow in the form of a vortex pair is evident in figure 15(a). Figures 15(b) to 15(h) also shows contour plots of all budget mechanisms at the upstream location along the corner. The pressure strain, normally inactive along the span in the viscous sublayer, has a positive contribution in the corner bisector budget. Distinct weakening of molecular diffusion and dissipation can be seen near the corner.

Further inspection of figure 14(c) shows that towards the end of the buffer layer ($y^+ \sim 20$), all mechanisms in the budget seem to approach zero. This inactive layer straddles the corner along each wall up to $y = z = 0.3$ and can be seen in figures 15(c) and 15(g). Beyond this inflection point, the production grows to a value larger than the centerline. The turbulent diffusion also briefly grows before abruptly becoming negative and, along with pressure diffusion and pressure strain, balances production. This activity coincides with the region of large strain and turbulent fluctuations, which occur in the buffer layer for the core span ($1.0 \leq z \leq 16.0$). Interestingly, as production grows, so do convection and the sum which indicates unsteadiness or a lag in the balancing of the mechanisms.

Reynolds-stress budget calculations along corner bisector are a rarity in the literature. Huser et al.[7] studied bisector budgets in a fully developed turbulent square duct, where DNS calculations were performed using high-order finite difference and the Fourier pseudo-spectral methods. The viscous sublayer behavior shown here was absent in their work. They showed that molecular diffusion, pressure strain, and dissipation were zero at the corner origin and grew marginally in the viscous sublayer. Also, production was balanced by dissipation in the buffer layer. This could be explained by the fact that no separation was present in the corner, thus only a limited outward shift of the peak production along the bisector. Unfortunately, the domain of ensembled mean data in the present work did not extend forward of the beginning of the corner separation, and thus did not afford an opportunity to validate bisector budgets in the non-separated corner.

The changes in the centerline $\overline{\rho u'' u''}$ beyond the reflected-shock foot (figure 14(b)) closely resemble that of the periodic SBLI shown in Vyas et al.[21] The location $(x - x_{imp}) = -3.7$, although downstream of the reflected-shock foot, shows no separation and the flow remains attached. Thus, isolating effects of the reflected shock from the eventual separation downstream. At the wall, dissipation jointly balances molecular diffusion and pressure strain. The peak production relocates to the log-law region and grows by more than twofold. Contrasting the behavior along the centerline with the corner in figure 14(d), a reduction in production is observed along with diminishing of complementary mechanisms. This is explained by weakening of the adverse pressure gradient from the centerline to the corner. In the viscous sublayer, key mechanisms at the upstream location continue to follow the trend, where dissipation and molecular diffusion jointly balances pressure strain. Thus, the results show a clear presence of two distinct mechanisms in the viscous sublayer and log-law region with an inflection point at $y^+ \sim 30$.

IV.C.2. Spanwise variations in the budget

To examine spanwise variations, the centerline ($z = 8.5$), quarter-span ($z = 3.7$), and corner bisector budgets were compared for two key Reynolds stresses, $\overline{\rho u'' u''}$ and $\overline{\rho u'' v''}$. In order to closely investigate each mechanism, only two are considered at a time, production and dissipation (figure 16), molecular and turbulent diffusion (figure 17), and pressure diffusion and pressure strain (figure 18).
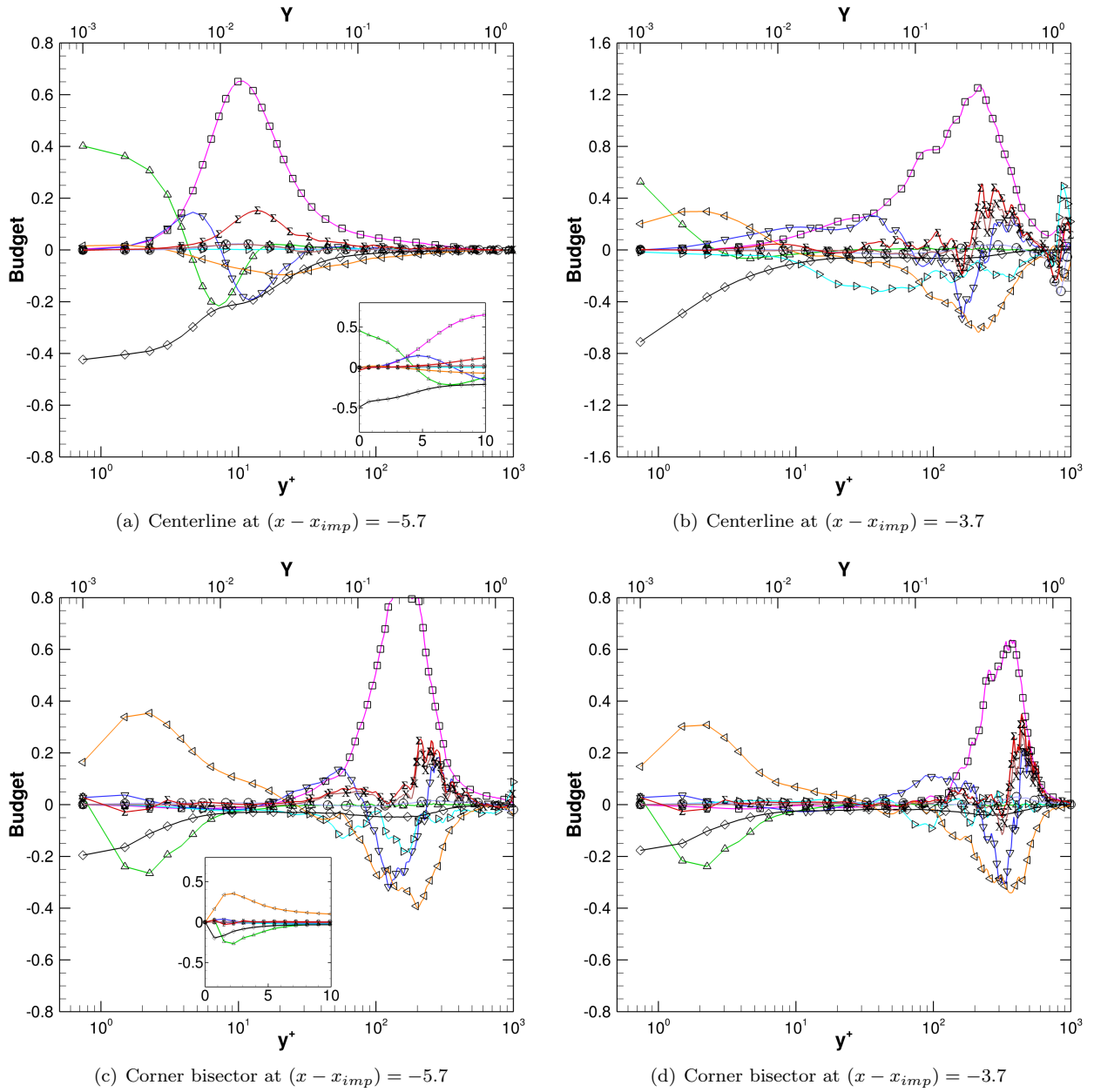
(a) Centerline at $(x - x_{imp}) = -5.7$

(b) Centerline at $(x - x_{imp}) = -3.7$

(c) Corner bisector at $(x - x_{imp}) = -5.7$

(d) Corner bisector at $(x - x_{imp}) = -3.7$

Figure 14. Budget of $\overline{\rho u'' u''}$. Normalized by $\rho_w u_\tau^4 / \nu_w$ at $(x - x_{imp}) = -5.7$. □: Production, △: Molecular diffusion, ▽: Turbulent diffusion, ▷: Pressure diffusion, ◁: Pressure strain, ◇: dissipation, ◯: Turbulent mass flux, X: Convection, and Σ: Sum.

Production and dissipation mechanisms for $\overline{\rho u'' u''}$ in figures 16(a) and 16(b) show that at upstream locations the mechanisms fall in two categories, the core span and the corner. In the core, mechanisms at the centerline and quarter-span are identical in behavior and magnitude. However, beyond the reflected-shock foot, the mechanisms fall in three distinct categories. Along the centerline, there is an increase in production and the peak shifts from the buffer layer to the log-law region ($y^+ \sim 200$). At quarter-span, evidence of a diminished peak in production exists in the buffer layer, but a prominent peak is present in the log-law region ($y^+ \sim 100$) with magnitude still at pre-reflected-shock level. Finally, the production in the corner bisector has a peak in the log-law region and of approximately the same magnitude as the quarter-span peak production, thus somewhat diminished from pre-reflected-shock level. The dissipation mechanism follows the above trend, i.e. quarter-span is similar to the centerline at upstream undisturbed core locations, but deviates from that behavior in the post-reflected-shock region, albeit, not as drastically as the production mechanism. The production and dissipation mechanisms for $\overline{\rho u'' v''}$ in figures 16(c) and 16(d) show that

similar to $\overline{\rho u''u''}$, production is more sensitive to the span than the dissipation. Figures 19 and 20 show contours of these mechanisms for the $\overline{\rho u''u''}$ and $\overline{\rho u''v''}$ components at the post-reflected-shock location of $(x - x_{imp}) = -3.7$. The goal is to distinguish the relative trends and not the magnitude, so the legends are clipped at $[-0.4, 0.4]$. Thus, providing a deeper insight in spanwise evolution of budgets.

The molecular and turbulent diffusion mechanisms for $\overline{\rho u''u''}$ and $\overline{\rho u''v''}$ are presented in figure 17. It is apparent that the molecular diffusion shows negligible change with varying span location in the regions where the flow remained attached. Since this mechanism relies on molecular viscosity, variations should be small in attached regions. For $\overline{\rho u''u''}$, the behavior along the corner bisector particularly stands out. As discussed in section IV.C.1., at the wall it is zero, but turns negative in the viscous sublayer. This is believed to be relocation of the trough, originally in the buffer layer, closer to the wall as the isotach curvature changes and moves closer to the corner origin. This can be seen by a careful observation of figure 15(e). The molecular diffusion mechanism for $\overline{\rho u''v''}$ show a similar trend, effectively switching signs in the viscous sublayer. The turbulent diffusion mechanism followed suit in the upstream locations, however in the post-reflected-shock region, spanwise variations develop due to the presence of recirculation regions at the midspan and corner, which increases spanwise transport inbetween the recirculation zones or above them by flow lifting off. This results in a broad turbulent diffusion region across the buffer layer followed by an immediate sink for the $\overline{\rho u''u''}$ component. The $\overline{\rho u''v''}$ component shows the opposite behavior in the core span, where the turbulent diffusion becomes negative. This leads to a negative-positive-negative wall normal distribution in contrast to positive-negative-positive for $\overline{\rho u''u''}$ component. This is clearly seen by comparing figures 19(e) and 20(e).

Finally, the pressure diffusion and pressure strain mechanisms are shown in figure 18. The variations are minimal for both at the upstream location in the core span. As seen earlier, the molecular diffusion balances pressure strain along the corner bisector for $\overline{\rho u''u''}$, however that role is taken on by pressure diffusion for $\overline{\rho u''v''}$. Also the magnitudes of these mechanisms are three times larger along the corner bisector than the core span for $\overline{\rho u''v''}$. Downstream of the reflected shock, a large increase in the core budgets is seen within the viscous sublayer, however the corner bisector maintains its pre-reflected-shock levels, suggesting that the corner origin is not influenced by the adverse pressure gradient. This is readily confirmed by figure 20(a), which shows two counter-rotating vortices along the bottom wall. Furthermore regarding the core budgets, the wall peak in both mechanisms is larger at the quarter-span owing to strong transverse velocity gradients in the viscous sublayer. But in the buffer layer, peaks in both mechanisms occur along the centerline due to the strong pressure gradient.

V.   Conclusions

Implicit large-eddy simulations were performed of an impinging shock-wave/boundary-layer interaction with a wall-resolved mesh. The flow conditions were based on wind tunnel experiments and hence the entire span, including the two sidewalls, was simulated to capture corner effects which result in spanwise variations of the Reynolds-stress transport budgets.

Detailed comparisons were made with particle image velocimetry, laser Doppler anemometry, and hot wire anemometry experimental data. The interaction length was found to be larger than the experiment by approximately $0.6\delta_{99}$, while the separation length was larger by $1.5\delta_{99}$. The mismatch of turbulent fluctuations, namely $\sqrt{\overline{u'u'}}$, in the outer portion of the upstream boundary layer is thought to be responsible for the discrepancy in these lengths. Skin friction in the upstream and reattached regions matched well with the experiment, although the reattachment was delayed. The weighted power spectral density was computed for a rake of pressures immediately downstream of the reflected-shock foot. Comparison with experimental power spectra showed that the peak power in the signal was comparable to the experiment, however the peak occured at $St_{Lint} = 0.01$ owing to the larger interaction region, which led to longer periods of separation growth and collapse cycles.

The Reynolds-stress budgets along the centerline compared well with the past budgets calculated in a quasi-2D impinging SBLI using periodic boundary conditions.[21] Infrequent and not widely available in the literature, budgets along the span and corner bisector were also calculated to examine the spanwise variation. Coupling of the corner separation and secondary flow showed new behavior in the viscous sublayer along the corner bisector, where the pressure gradient mechanism had positive contribution and was jointly balanced by negative molecular diffusion and dissipation. An inflection point, located at the end of the buffer layer and beginning of the log-law region, was found in the corner bisector where all mechanisms approached zero.

Regarding the spanwise variations, the budgets could be categorized by two distinct behaviors upstream

of the reflected shock—the core span and corner bisector. Downstream of the reflected-shock foot, the budgets fell into three categories; the two previously mentioned and the new behavior in the region between the centerline and corner separations. Production, turbulent diffusion, pressure diffusion, and pressure strain mechanisms showed the largest variation downstream of the reflected shock for $\overline{\rho u'' u''}$ and $\overline{\rho u'' v''}$.

References

[1] Dolling, D. S., "Fifty Years of Shock-Wave/Boundary-Layer Interaction Research: What Next?" *AIAA Journal*, Vol. 39, No. 8, August 2001, pp. 1517–1531.

[2] Zheltovodov, A. A., "Some Advances in Research of Shock Wave/Turbulent Boundary-layer Interactions," No. 2006-0496 in 44th Aerospace Sciences Meeting, American Institute of Aeronautics and Astronautics, January 2006.

[3] Gaitonde, D. V., "Progress in Shock Wave/Boundary Layer Interactions," No. 2013-2607 in 43rd Fluid Dynamics Conference, American Institute of Aeronautics and Astronautics, June 2013.

[4] Dussauge, J.-P., Dupont, P., and Debiève, J.-F., "Unsteadiness in Shock Wave Boundary Layer Interactions with Separations," *Aerospace Science and Technology*, Vol. 10, No. 2, December 2006, pp. 85–91.

[5] Souverein, L. J., Dupont, P., Debiève, J.-F., Dussauge, J.-P., van Oudheusden, B. W., and Scarano, F., "Effect of Interaction Strength on Unsteadiness in Turbulent Shock Wave Induced Separations," *AIAA Journal*, Vol. 48, No. 7, July 2010, pp. 1480–1493.

[6] Spalart, P. R., "Direct Simulation of a Turbulent Boundary Layer up to $R_\theta = 1410$," *Journal of Fluid Mechanics*, Vol. 187, May 1988, pp. 61–98.

[7] Huser, A., Biringen, S., and Hatay, F. F., "Direct Numerical Simulation of Turbulent Flow in a Square Duct: Reynolds Stress Budgets," No. 1994-0187 in 32nd Aerospace Sciences Meeting, American Institute of Aeronautics and Astronautics, January 1994.

[8] Hamlington, P. E. and Dahm, W. J. A., "Reynolds Stress Closure for Nonequilibrium Effects in Turbulent Flows," *Physics of Fluids*, Vol. 20, No. 11, November 2008.

[9] Mansour, N. N., Kim, J., and Moin, P., "Reynolds Stress and Dissipation Rate Budgets in a Turbulent Channel Flow," *Journal of Fluid Mechanics*, Vol. 194, June 1988, pp. 15–44.

[10] Clemens, N. T. and Narayanaswamy, V., "Low-frequency Unsteadiness of Shock Wave/Turbulent Boundary Layer Interactions," *The Annual Review of Fluid Mechanics*, Vol. 46, January 2014, pp. 469–492.

[11] Gonsalez, J. C. and Dolling, D. S., "Correlation of Interaction Sweepback Effects on the Dynamics of Shock-Induced Turbulent Separation," No. 1993-0776 in 31th Aerospace Sciences Meeting, American Institute of Aeronautics and Astronautics, January 1993.

[12] Georgiadis, N. J., Rizzetta, D. P., and Fureby, C., "Large-eddy Simulations: Current Capabilities, Recommended Practices, and Future Research," *AIAA Journal*, Vol. 48, No. 8, August 2010, pp. 1772–1784.

[13] Gaitonde, D. V. and Visbal, M. R., "Padé-type Higher-order Boundary Filters for the Navier-Stokes Equations," *AIAA Journal*, Vol. 38, No. 11, November 2000, pp. 2103–2112.

[14] Visbal, M. R., Morgan, P. E., and Rizzetta, D. P., "An Implicit LES Approach Based on High-order Compact Differencing and Filterning Schemes," No. 2003-4098 in 16th Computational Fluid Dynamics Conference, American Institute of Aeronautics and Astronautics, June 2003.

[15] Mathew, J., Lechner, R., Foysi, H., Sesterhenn, J., and Friedrich, R., "An Explicit Filtering Method for Large-eddy Simulation of Compressible Flows," *Physics of Fluids*, Vol. 15, No. 8, August 2003, pp. 2279–2289.

[16] Vyas, M. A., Waindim, M., and Gaitonde, D. V., "Budget of Turbulent Kinetic Energy in a Shock Wave/Boundary-layer Interaction," No. 2016-3187 in 46th Fluid Dynamics Conference, American Institute of Aeronautics and Astronautics, June 2016.

[17] Schiavo, L. A. C. A., de Jesus, A. B., Azevedo, J. L. F., and Wolf, W. R., "Adverse Pressure Gradient Effects in the Turbulent Kinetic Energy Budget for Channel Flows," No. 2015-1276 in 53rd Aerospace Sciences Meeting, American Institute of Aeronautics and Astronautics, January 2015.

[18] Pirozzoli, S. and Bernardini, M., "Direct Numerical Simulation Database for Impinging Shock Wave/Turbulent Boundary-layer Interaction," *AIAA Journal*, Vol. 49, No. 6, June 2011, pp. 1307–1312.

[19] Morgan, B., Duraisamy, K., Nguyen, N., Kawai, S., and Lele, S. K., "Flow Physics and RANS Modelling of Oblique Shock/Turbulent Boundary Layer Interaction," *Journal of Fluid Mechanics*, Vol. 729, July 2013, pp. 231–284.

[20] Wilcox, D. C., *Turbulence Modeling for CFD*, DCW Industries, Inc., 3rd ed., July 2010.

[21] Vyas, M. A., Yoder, D. A., and Gaitonde, D. V., "Reynolds-stress Budgets in an Impinging Shock Wave/Boundary-layer Interaction," No. 2018-1299 in 2018 AIAA Aerospace Sciences Meeting, American Institute of Aeronautics and Astronautics, January 2018.

^{22}Gaitonde, D. V. and Visbal, M. R., "High-order Schemes for Navier-Stokes Equations: Algorithm and Implementation into FDL3DI," Technical Report 3060, Air Force Research Laboratory, August 1998.

^{23}Anderson, D. A., Tannehill, J. C., and Pletcher, R. H., *Computational Fluid Mechanics and Heat Transfer*, Computational Methods in Mechanics and Thermal Sciences, Hemisphere Publishing Corporation, 1984.

^{24}Klein, M., Sadiki, A., and Janicka, J., "A Digital Filter Based Generation of Inflow Data for Spatially Developing Direct Numerical or Large Eddy Simulations," *Journal of Computational Physics*, Vol. 186, February 2003, pp. 652–665.

^{25}Veloudis, I., Yang, Z., McGuirk, J. J., Page, G. J., and Spencer, A., "Novel Implementation and Assessment of a Digital Filter Based Approach for the Generation of LES Inlet Conditions," *Flow, Turbulence and Combustion*, Vol. 79, March 2007, pp. 1–24.

^{26}Xie, Z.-T. and Castro, I. P., "Efficient Generation of Inflow Conditions for Large Eddy Simulation of Street-scale Flows," *Flow, Turbulence and Combustion*, Vol. 81, April 2008, pp. 449–470.

^{27}Pope, S. B., *Turbulent Flows*, Cambridge University Press, 8th ed., 2011.

^{28}Touber, E. and Sandham, N. D., "Oblique Shock Impinging on a Turbulent Boundary Layer: Low-Frequency Mechanisms," No. 2008-4170 in 38th Fluid Dynamics Conference, American Institute of Aeronautics and Astronautics, June 2008.

^{29}Lund, T. S., Wu, X., and Squires, K. D., "Generation of Turbulent Inflow Data for Spatially-developing Boundary-layer Simulations," *Journal of Computational Physics*, Vol. 140, 1998, pp. 233–258.

^{30}Gerolymos, G. A., "Implicit Multiple-grid Solution of the Compressible Navier-Stokes Equations Using $k - \epsilon$ Turbulence Closure," *AIAA Journal*, Vol. 28, No. 10, October 1990, pp. 1707–1717.

^{31}Guarini, S. E., Moser, R. D., Shariff, K., and Wray, A., "Direct Numerical Simulation of a Supersonic Turbulent Boundary Layer at Mach 2.5," *Journal of Fluid Mechanics*, Vol. 414, January 2000, pp. 1–33.

^{32}Lele, S. K., "Compact Finite Difference Scheme with Spectral-like Resolution," *Journal of Computational Physics*, Vol. 103, August 1992, pp. 16–42.

^{33}Visbal, M. R. and Gaitonde, D. V., "On the Use of High-order Finite-difference Schemes on Curvilinear and Deforming Meshes," *Journal of Computational Physics*, Vol. 181, May 2002, pp. 155–185.

^{34}Visbal, M. R. and Gaitonde, D. V., "Shock Capturing Using Compact-differencing-based Methods," No. 2005-1265 in 43rd Aerospace Sciences Meeting, American Institute of Aeronautics and Astronautics, January 2005.

^{35}Jiang, G.-S. and Shu, C.-W., "Efficient Implementation of Weighted ENO Schemes," *Journal of Computational Physics*, Vol. 126, No. 0130, January 1996, pp. 202–228.

^{36}Leer, B. V., "Towards the Ultimate Conservation Difference Scheme. V. A Second-order Sequel to Godunov's Method," *Journal of Computational Physics*, Vol. 32, July 1979, pp. 101–136.

^{37}Beam, R. M. and Warming, R. F., "An Implicit Factored Scheme for the Compressible Navier-Stokes Equations," *AIAA Journal*, Vol. 16, No. 4, April 1978, pp. 393–402.

^{38}Kawai, S., Shankar, S. K., and Lele, S. K., "Assessment of Localized Artificial Diffusivity Scheme for Large-eddy Simulation of Compressible Turbulent Flows," *Journal of Computational Physics*, Vol. 229, November 2010, pp. 1739–1762.

^{39}Garmann, D. J., Visbal, M. R., and Orkwis, P. D., "Comparative Study of Implicit and Subgrid-scale Model Large-eddy Simulation Techniques for Low-Reynolds Number Airfoil Applications," *International Journal for Numerical Methods in Fluids*, Vol. 71, August 2013, pp. 1546–1565.

^{40}Dussauge, J.-P., Dupont, P., Debiève, J.-F., Piponniau, S., and Souverein, L. J., "Experiments on Oblique Shock Reflections at M = 2.3 at IUSTI," Oral presentation at the Workshop On Shock Wave/Boundary-layer Interactions.

^{41}Garnier, E., Sagaut, P., and Deville, M., "Large Eddy Simulation of Shock/Boundary-layer Interaction," *AIAA Journal*, Vol. 40, No. 10, October 2002, pp. 1935–1944.

^{42}Babinsky, H., Oorebeek, J., and Cottingham, T. G., "Corner Effects in Reflecting Oblique Shock-wave/Boundary-layer Interactions," No. 2013-0859 in 51st Aerospace Sciences Meeting, American Institute of Aeronautics and Astronautics, January 2013.

^{43}Agostini, L., Larchevêque, L., Dupont, P., Debiève, J.-F., and Dussauge, J.-P., "Zones of Influence and Shock Motion in a Shock/Boundary-layer Interaction," *AIAA Journal*, Vol. 50, No. 6, June 2012, pp. 1377–1387.

^{44}Georgiadis, N. J., Vyas, M. A., and Yoder, D. A., "Wind-US Code Contribution to the First AIAA Shock Boundary Layer Interaction Prediction Workshop," Technical Memorandum 2013-217837, NASA Glenn Research Center, February 2013.

^{45}DeBonis, J. R., Oberkampf, W. L., Wolf, R. T., Orkwis, P. D., Turner, M. G., Babinsky, H., and Benek, J. A., "Assessment of Computational Fluid Dyanmics and Experimental Data for Shock Boundary-layer Interactions," *AIAA Journal*, Vol. 50, No. 4, April 2012, pp. 891–903.

^{46}Touber, E. and Sandham, N. D., "Large-eddy Simulations of Low-frequency Unsteadiness in a Turbulent Shock-induced Separation Bubble," *Theoretical and Computational Fluid Dynamics*, Vol. 23, May 2009, pp. 79–107.
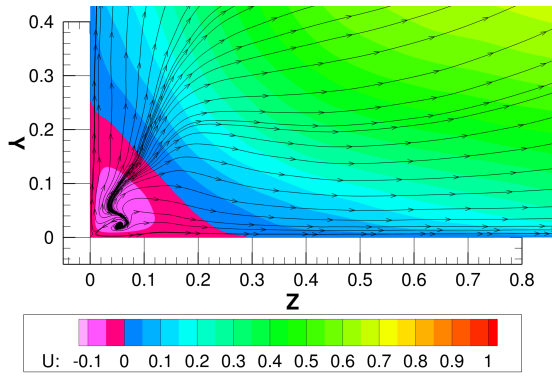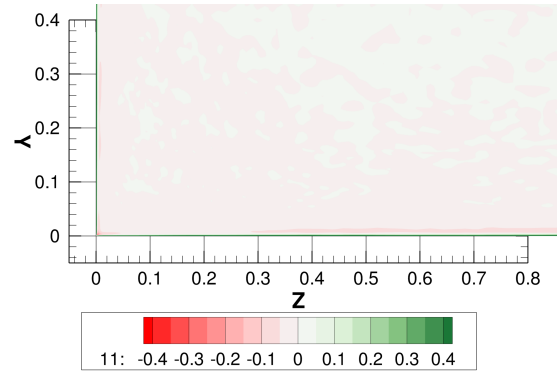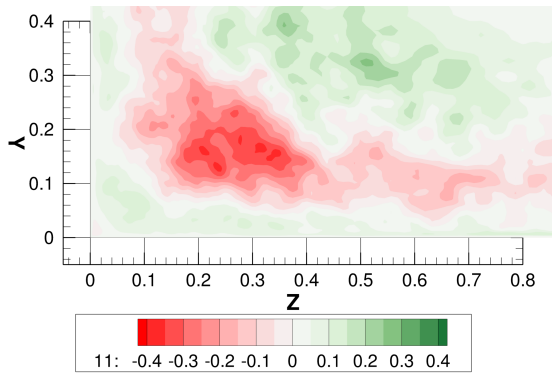
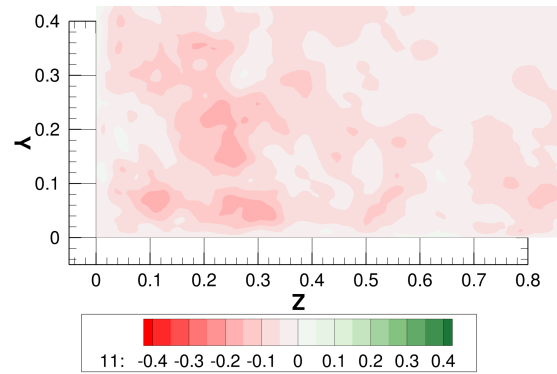(a) Streamwise velocity with planar streamlines
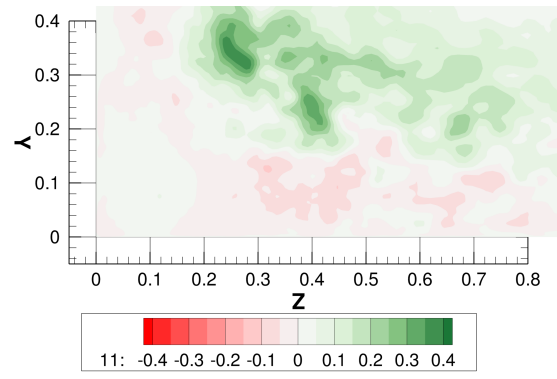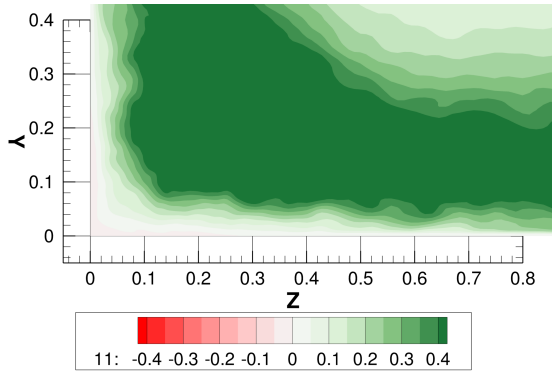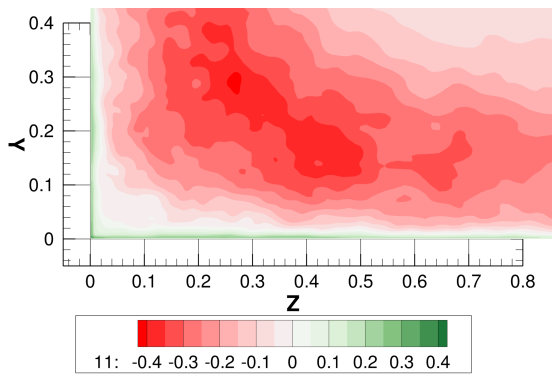
(b) Convection

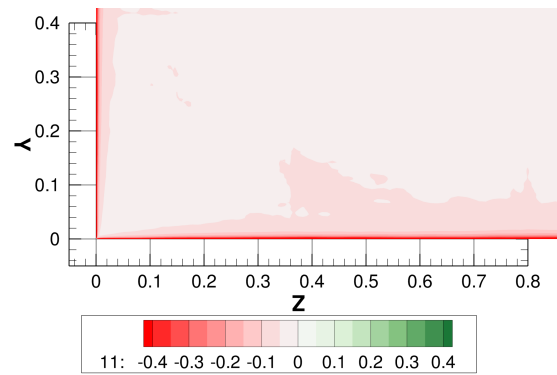(c) Production

(d) Molecular Diffusion
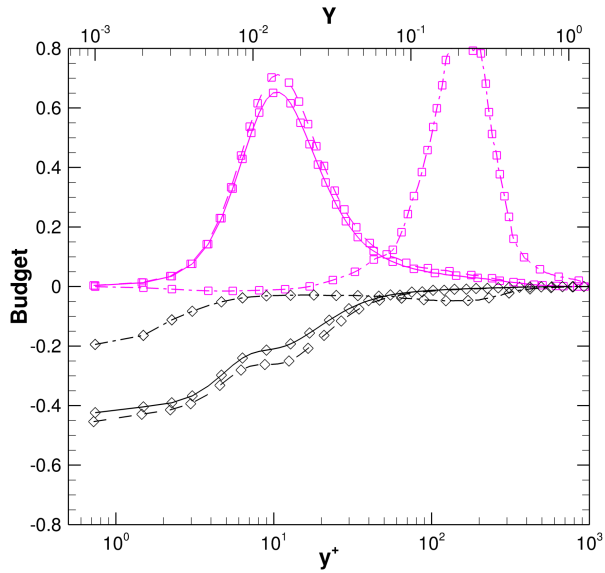
(e) Turbulent Diffusion
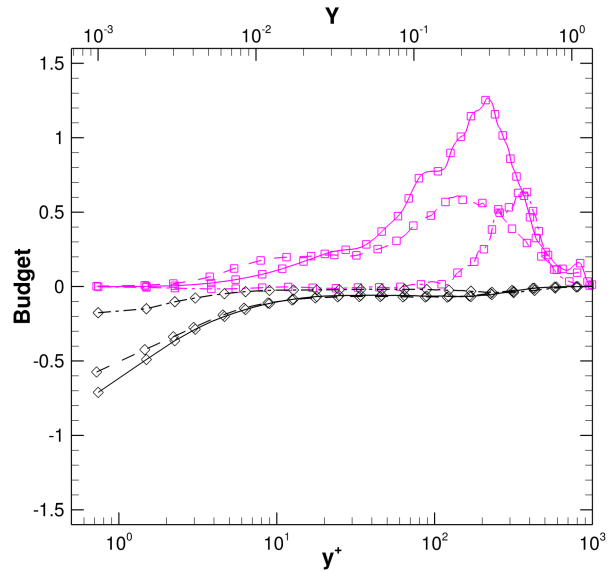
(f) Pressure Diffusion

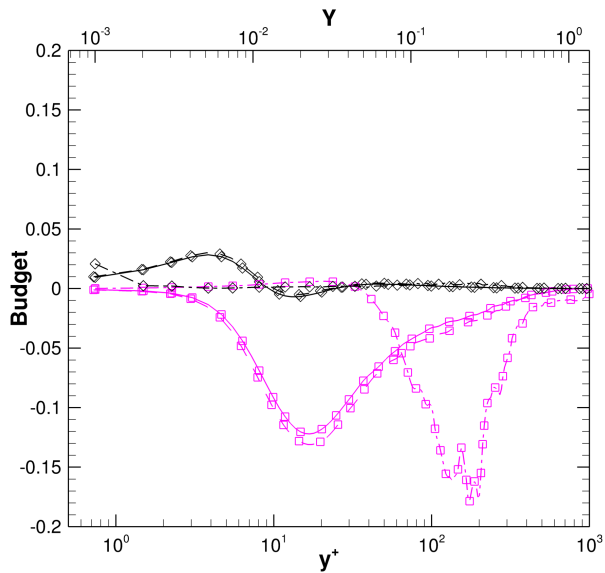(g) Pressure Strain

(h) Dissipation

Figure 15. Contours of streamwise velocity and $\overline{\rho u'' u''}$ budget mechanisms at $(x - x_{imp}) = -5.7$. Normalized by $\rho_w u_\tau^4 / \nu_w$ at $(x - x_{imp}) = -5.7$.
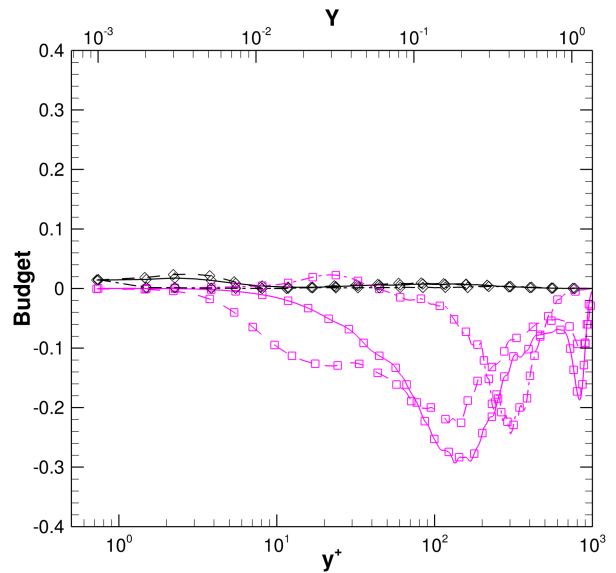
(a) $\overline{\rho u'' u''}$ at $(x - x_{imp}) = -5.7$
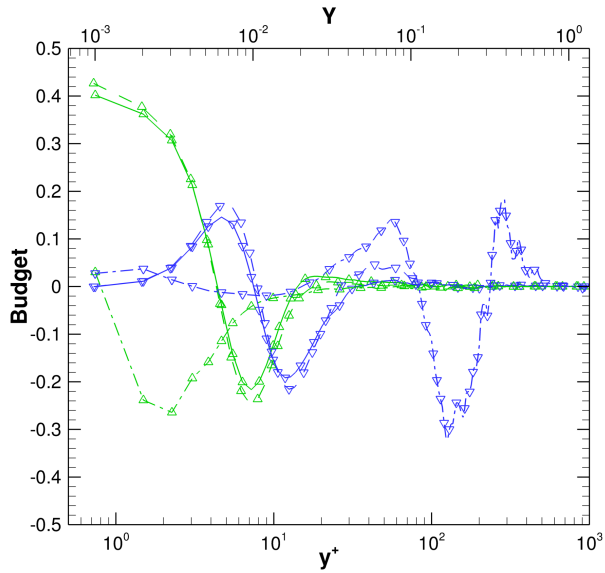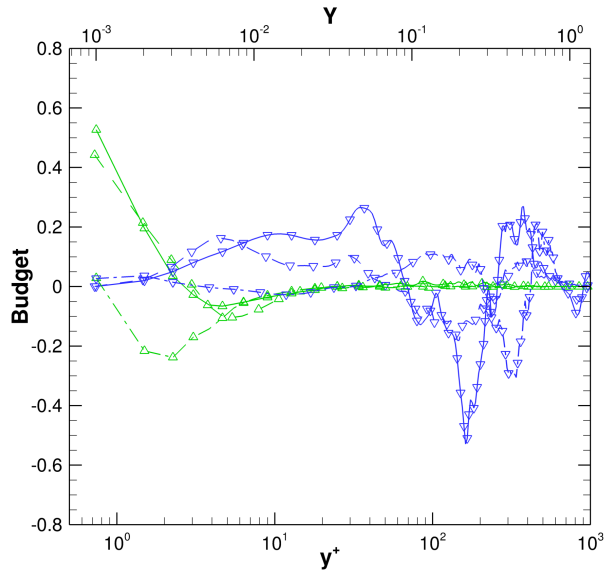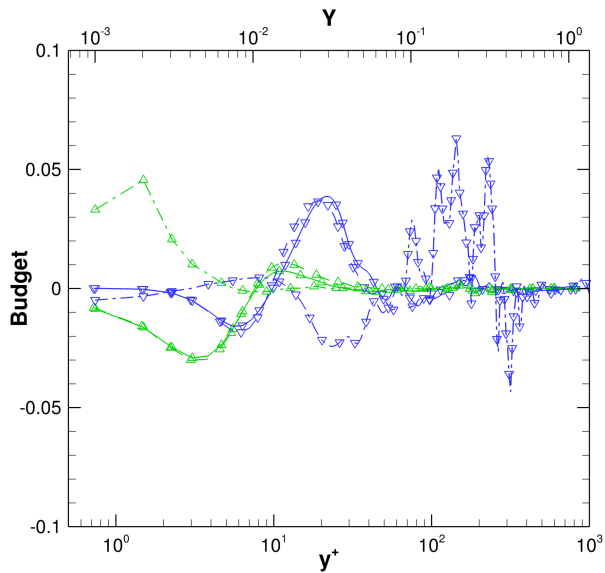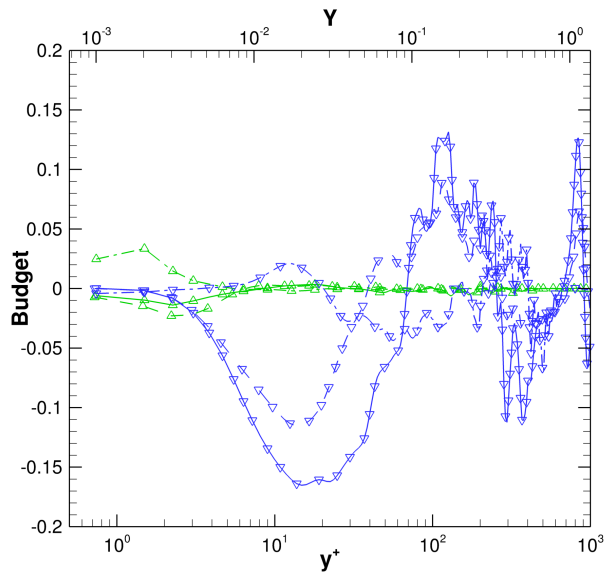
(b) $\overline{\rho u'' u''}$ at $(x - x_{imp}) = -3.7$

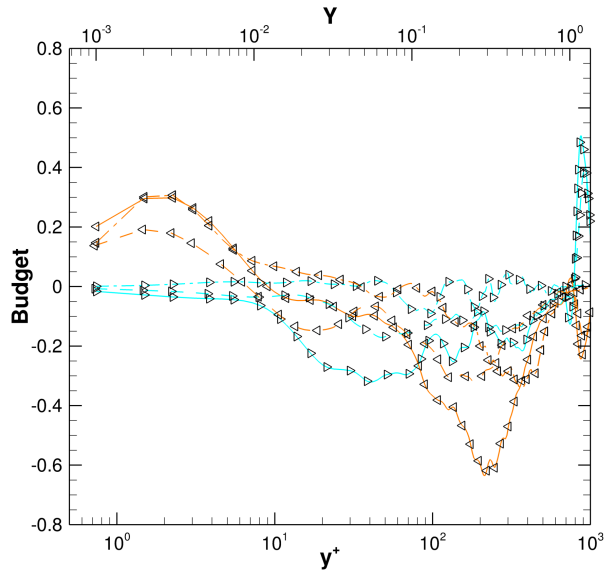(c) $\overline{\rho u'' v''}$ at $(x - x_{imp}) = -5.7$

(d) $\overline{\rho u'' v''}$ at $(x - x_{imp}) = -3.7$

Figure 16. Production and dissipation budgets along the centerline (solid), quarter-span (dash), and corner bisector (dash dot). Normalized by $\rho_w u_\tau^4 / \nu_w$ at $(x - x_{imp})$. $\square$: Production and $\lozenge$: dissipation.
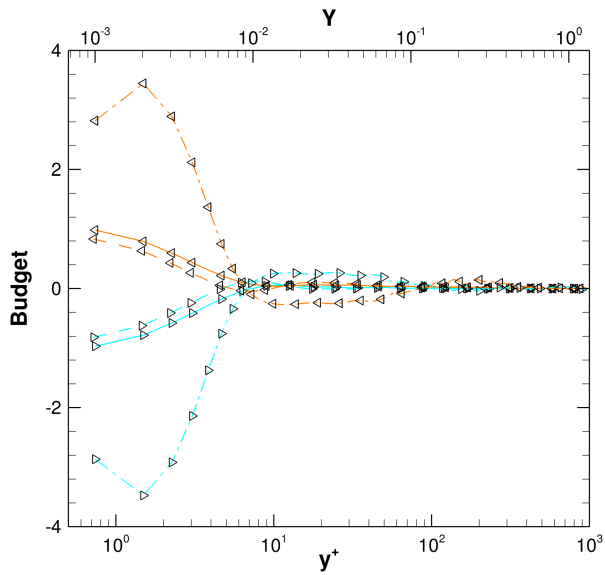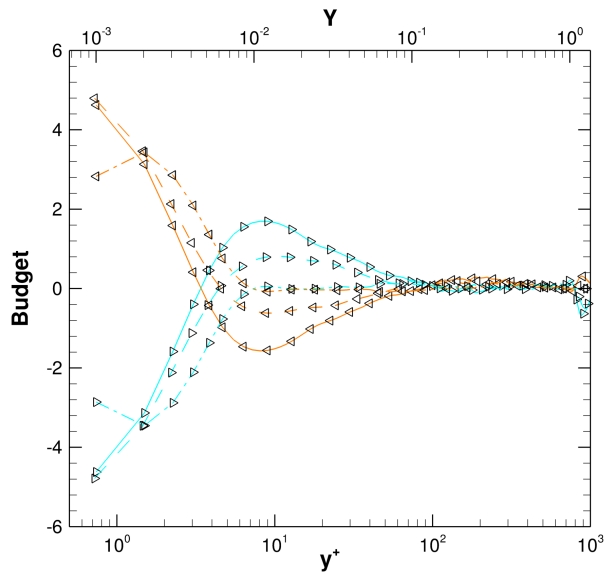
Figure 17. Molecular and turbulent diffusion budgets along the centerline (solid), quarter-span (dash), and corner bisector (dash dot). Normalized by $\rho_w u_\tau^4/\nu_w$ at $(x - x_{imp}) = -5.7$. △: Molecular diffusion and ▽: Turbulent diffusion.

Figure 18. Pressure diffusion and pressure strain budgets along the centerline (solid), quarter-span (dash), and corner bisector (dash dot). Normalized by $\rho_w u_\tau^4 / \nu_w$ at $(x - x_{imp}) = -5.7$. ▷: Pressure diffusion and ◁: Pressure strain.

(a) Streamwise velocity with planar streamlines

(b) Convection

(c) Production

(d) Molecular Diffusion

(e) Turbulent Diffusion

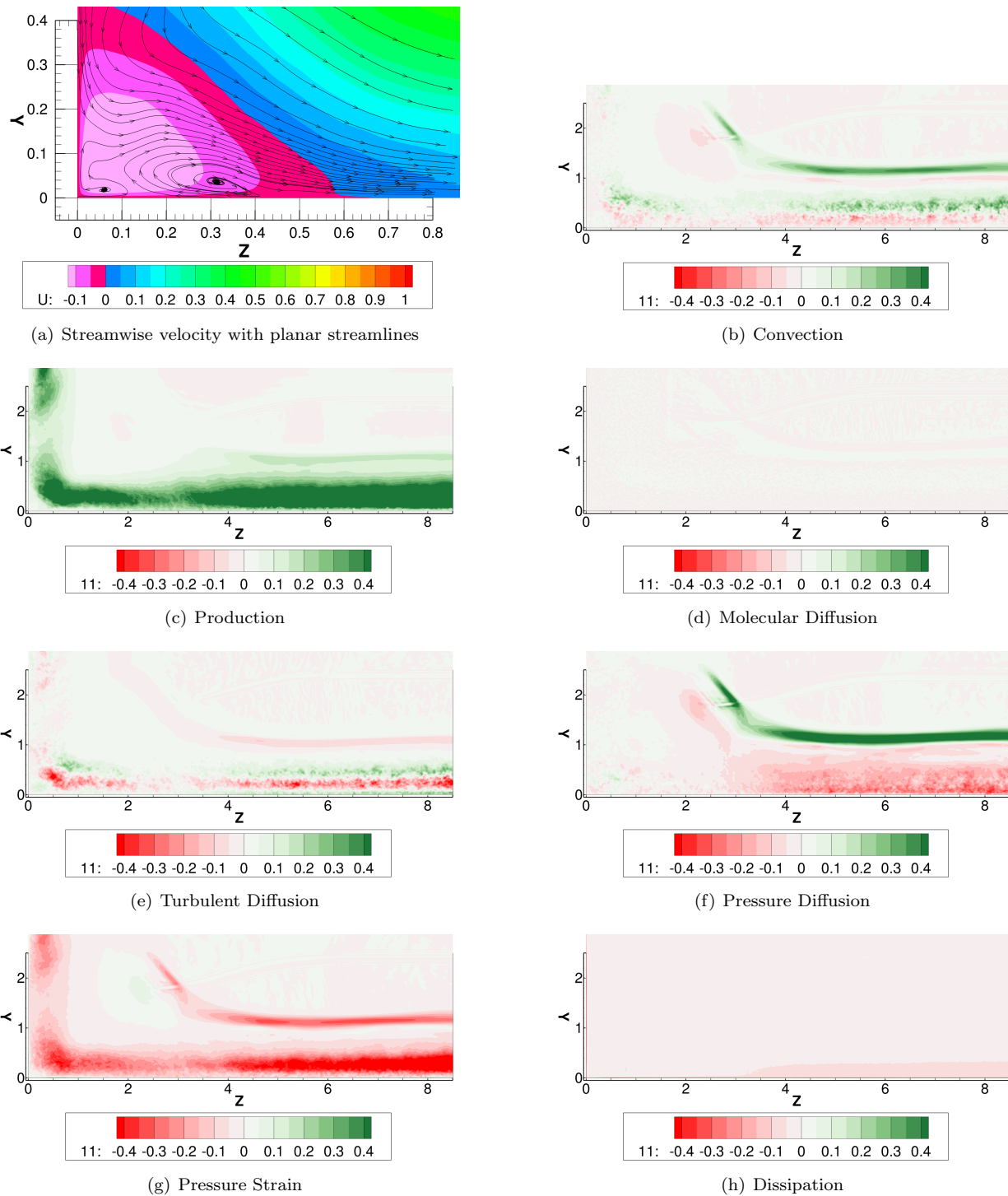(f) Pressure Diffusion

(g) Pressure Strain

(h) Dissipation

Figure 19. Contours of streamwise velocity and $\overline{\rho u'' u''}$ budget mechanisms at $(x - x_{imp}) = -3.7$. Normalized by $\rho_w u_\tau^4 / \nu_w$ at $(x - x_{imp}) = -5.7$.

(a) Streamwise velocity with planar streamlines

(b) Convection

(c) Production

(d) Molecular Diffusion

(e) Turbulent Diffusion

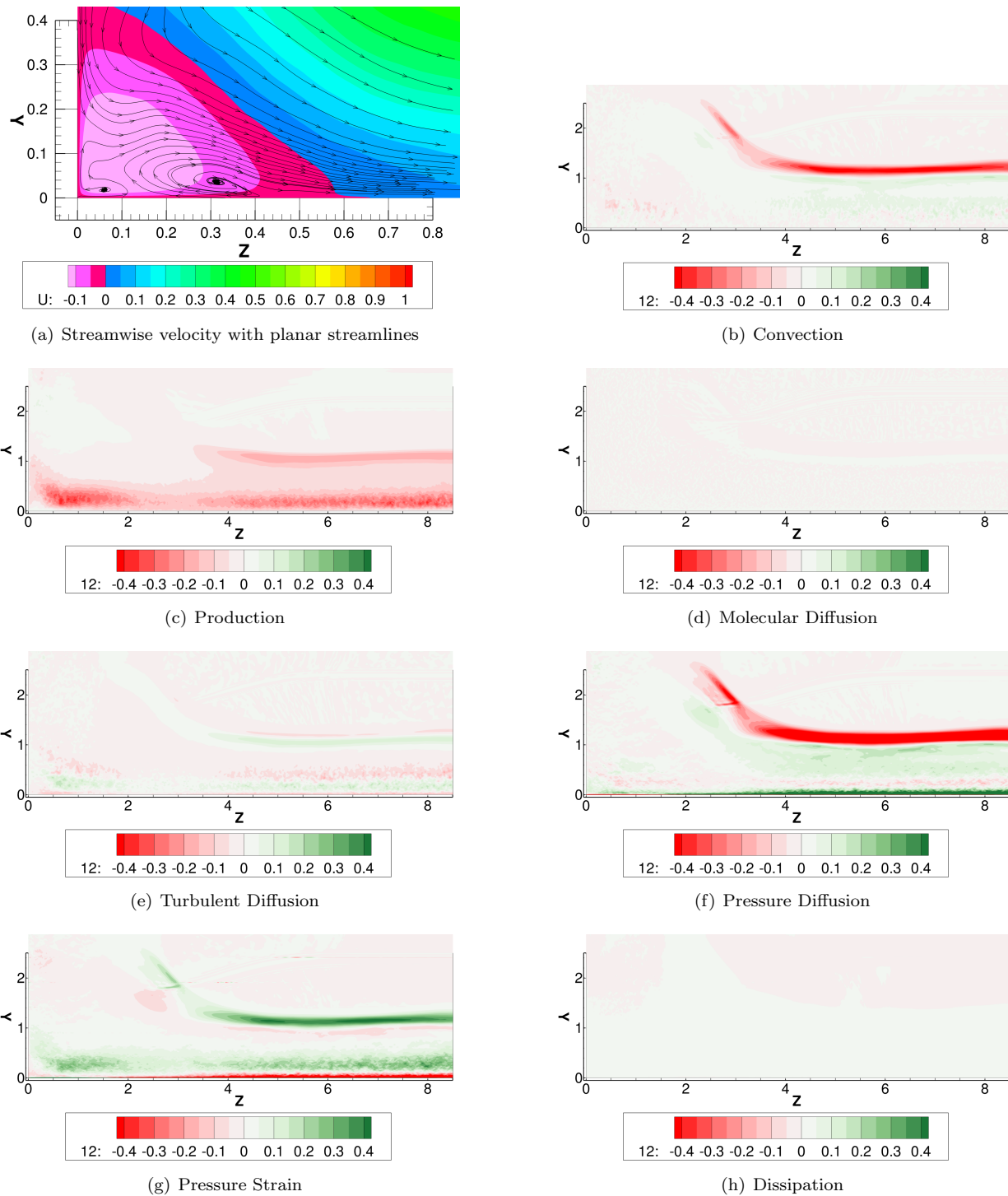(f) Pressure Diffusion

(g) Pressure Strain

(h) Dissipation

Figure 20. Contours of streamwise velocity and $\overline{\rho u'' v''}$ budget mechanisms at $(x - x_{imp}) = -3.7$. Normalized by $\rho_w u_\tau^4 / \nu_w$ at $(x - x_{imp}) = -5.7$.